Doctoral Thesis

Stability Enhancement in Solution-Processed Perovskite Solar Cells

Sandeep Kajal

Department of Chemistry

Graduate School of UNIST

2020

Doctoral Thesis

Stability Enhancement in Solution-Processed Perovskite Solar Cells

Sandeep Kajal

Department of Chemistry

Graduate School of UNIST

2020

Stability Enhancement in Solution-Processed Perovskite Solar Cells

A thesis/dissertation

submitted to the Graduate School of UNIST

in partial fulfillment of the

requirements for the degree of

Doctor of Philosophy

Sandeep Kajal

May 08/2020

Approved by

Advisor

Prof. Kwang Soo Kim

Stability Enhancement in Solution-Processed Perovskite Solar Cells

Sandeep Kajal

This certifies that the thesis/dissertation of Sandeep Kajal is

Approved

May 08/2020

Advisor: Prof. Kwang Soo Kim

Prof. Jin Young Kim: Thesis Committee Member

Prof. Tae-Hyuk Kwon: Thesis Committee Member

Prof. Geunsik Lee: Thesis Committee Member

Prof. Gi-Hwan Kim: Thesis Committee Member

Abstract

The high cost and complexity of fabrication in silicon based photovoltaic (PV) provoked considerable research interest for alternative solution-processed photovoltaic solar cells. Organic-inorganic perovskite solar cells gained attention as they high defect tolerance, high absorption coefficient, low defect density, long diffusion lengths, and low low-exciton binding energy, also they achieved comparable higher efficiency than single junction Si-solar cells. However, compared to the established PV technologies, organic-inorganic perovskite solar cells lacks in terms of stability and degrades easily under the influence of light, humidity, and moisture. All-inorganic solar cells offer better thermal and photo-stability compared to their counterpart perovskite solar cells because they have non-volatile compounds in their 3D lattice structure. The structural and air stability of $CsPbI_3$ is hindering the researchers to explore the full potential but addition of excess HI or zwitterions assisted methods solved the structural issue to some extent. This thesis aims to solve stability issues in perovskite materials and find their application in highly efficient optoelectronic devices.

In the 1st chapter, we introduced in detail, the basic properties of perovskite material, the essential parameters of solar cells, the device architecture, and the mechanism related to perovskite degradation. Also, we discussed the previous techniques to improve the stability in different structures of perovskite solar cells. The 2nd chapter of this thesis aims to stabilize α-$CsPbI_3$ using barium doping, and its application in optoelectronic devices. In this part, we briefly introduced the general background, metastable behavior. Also our approach for the surface passivated, Ba-doped α-$CsPbI_3$ exhibit thermal stablity upon annealing as well as highly photo-stable over a year, and it also exhibits ~1.72 eV band gap suitable for optoelectronic applications. All inorganic solar cells based on the Ba-doped α-$CsPbI_3$ retain 98% of its initial PCE values even after 700 hours, also the red light-emitting diodes (LED) exhibit the light emission at 700 nm with bandwidth 39 nm.

In the 3rd chapter, we unfolded the effect of metal doping on the properties of $CsPbI_3$ perovskite by using theory and experimental evidences. The heterovalent metals (i.e. Bi^{3+}, Sb^{3+}) and divalent cations (i.e., Ba^{2+}, Sr^{2+}, and Sn^{2+}) were doped to stabilize the α-$CsPbI_3$ by replacing the Pb^{2+} cations. We challenged the earlier assumptions of stabilizing α-$CsPbI_3$ by heterovalent doping and we demonstrated that the divalent cations stabilize α-$CsPbI_3$ films, making thermally stable at high temperatures, whereas heterovalent metal-doping stabilizes β-$CsPbI_3$ films, making metastable. Also, we propose that Sr doping is more favorable for device fabrication because of its better charge dissociation and transport kinetics compared to Ba doped and α-$CsPbI_3$ perovskite films.

In the 4th chapter, we discussed the newly synthesize sulfonated octylammonium materials for passivating the perovskite crystal grain interface to stop ion migration. We incorporate three different octyl-ammonium sulfate compounds, Octylamine functionalized with sulfanilic acid (OAS), p-toluene sulfonic acid (OAT), and camphor sulfonic acid (OAC). We demonstrate that, passivating the grains

interface reduces the hysteresis, improves charge recombination and the stability, and also achieved the power conversion efficiency of 18.56% for the control device to 18.26%, 22.09%, and 21.5% for OAS, OAT, and OAC, respectively.

Table of Contents

List of Figures

Abbreviations

PV: Photovoltaic

3D: Three dimensional

HI: Hydroiodic acid

Ba: Barium

LED: Light-emitting diodes

OAS: Octylamine functionalized with sulfanilic acid

OAT: Octylamine functionalized with p-toluene sulfonic acid

OAC: Octylamine functionalized with camphor sulfonic acid

PSC: Perovskite solar cells

PCE: Power conversion efficiency

HP: Halide perovskite

MA: Methylammonium

FA: Formamidinium

t: Goldschmidt's tolerance factor

μ: Octahedral factor

IV: Current-Voltage

I_{SC}: Short-circuit current

V_{OC}: Open circuit voltage

FF: Fill factor

η: Efficiency

P*max:* Maximum power

DSCs: Dye-sensitized solar cells

LUMO: Lowest unoccupied molecular orbital

HTL: Hole transporting layer

ETL: Electron transporting layer

TGA: Thermogravimatric analysis

CSA: Camphor sulfonic acid

DFT: Density functional theory

P3HT: 3-hexylthiophene-2,5diyl

EQE: External quantum efficiency

FWHM: Full width at half maximum

BaI_2: Barium Iodide, PbI_2: lead iodide, DMSO: dimethyl sulfoxide

CB: Chlorobenzene, DMF: N,N-dimethylformamide

J–V: current density–voltage

E_f: Formation energy, PL: Photoluminiscence

FESEM: Field emission scanning electron microscope

NMR: Nuclear magnetic resonance spectroscopy

FT-IR: Fourier transform infrared spectroscopy

XPS: X-ray photoelectron spectroscopy

HPXRD: High power X-ray diffraction

TCSPC: Time-Correlated Single Photon Counting

TOF-SIMS: Time-of-Flight secondary ion mass spectrometry

Jsc: Short Circuit Current Density

IPCE: Incident Photon to Current Efficiency

J-V-L: Current density-voltage-luminance

CIE: International Commission on Illumination

Chapter 1

Background

Energy is an important source of human survival and civilization. There is a massive requirement of energy for human development, and the demand is directly correlated with the development of a nation. There has been a gradual increase in global energy consumption. This global energy demand alarmed the humankind for a big challenge in the 21st century. Most of the energy consumption was fulfilled by fossil fuels like oil, coal, and gas so far, and the burning of fossil fuels produces the so-called greenhouse gases like (CO_2). The extinction of fossil fuels and environmental pollution concerns lead the researchers to search for clean and renewable energy sources. Solar energy can be converted to electrical energy using a device called photovoltaic (PV), and the sunlight is the most abundant natural resource that can help humankind to meet their future energy demands. PV employs semiconductor materials for the conversion of sunlight to electricity. Silicon-based PV is among the most successfully commercialized PV technologies to date but their installation cost is high. Perovskite solar cells (PSC) gained the utmost attention as the most promising candidate for next-generation PV due to their high efficiency, low cost, and simple preparation process. After the first report in 2009, intensive research efforts made it possible to surpass the power conversion efficiency (PCE) to 25%, much higher than that of Si-based commercial devices. These halide perovskite (HP) bears a 3D structure with a denotation ABX_3, where A site can have any cation ((MA^+) , or (FA^+), or Cs^+), B can be any suitable metal ion (e.g., Pb^{2+}, Sn^{2+}), and X can be anions of the VII A group of periodic table namely I, Br, or Cl as shown in **Figure 1.1.** Empirically, the Goldschmidt's tolerance factor (t) and octahedral factor (μ) of ABX_3 structures are calculated by a factor as:

$$t = \frac{r_{A+}r_X}{\sqrt{2}\,(r_{B+}r_X)}$$

$$\mu = \frac{r_B}{r_X}$$

where, $r_{A,}r_X$, r_B are the corresponding radii of cation, halides, and the anion, respectively.

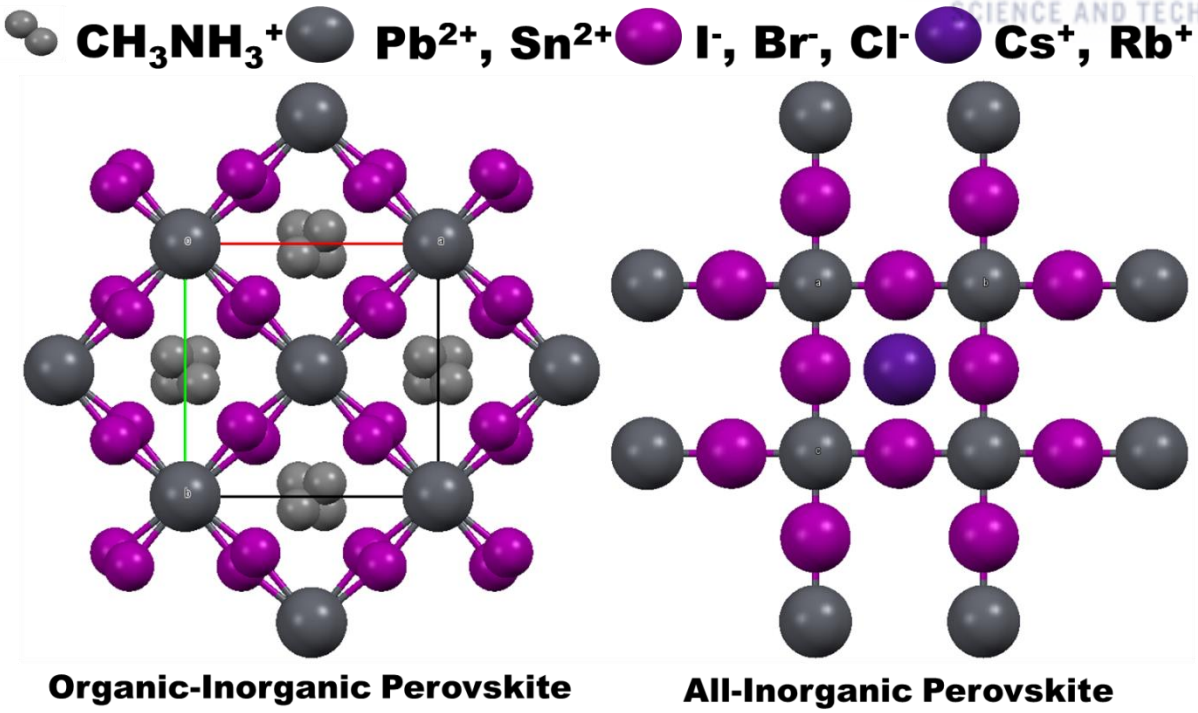

Figure 1.1. Schematic representation of perovskites structures. (a) ABX_3 crystal structure of organic-inorganic perovskites. (b) ABX_3 crystal structure of all-inorganic perovskites.

These factors are important to predict the type of crystal structure a perovskite acquires, for instance when t lies in between 0.8 and 1.0, the perovskite has a perfect 3D structure, whereas a value greater than 1.0 and less than 0.8 forms a non-perovskite phase. Eventually, μ lies in between the 0.4 to 0.9, which greatly restricts the numerous configurational possibilities; the ABX_3 nomenclature might possess to fewer combinations of A, B, and X leading to a stable BX_6 octahedra. Perovskite materials find its application in many optoelectronics devices because of its excellent optical and electrical properties.

1.1.Perovskite solar cell parameters

When light is illuminated over a cell it adds to the normal "dark" currents and it can be expressed by the diode law as follows:

$$I = I_o\left[exp\left(\frac{qV}{nkT}\right) - 1\right] - I_L$$

Where, I_L is light generated current.

While the diode equation for the IV curve in the first quadrant is:

$$I = I_L - I_o\left[exp\left(\frac{qV}{nkT}\right) - 1\right]$$

Usually the light generated current dominates the I_o (…) and the -1 term is neglected.

$$I=I_L- I_o\left[exp\left(\frac{qV}{nkT}\right)\right]$$

i) Short-circuit current density

The current generated and collected due to the light-generated carriers is termed as short circuit current (I_{SC}). It is the current through the perovskite solar cell when the voltage across it is zero. Usually, short-circuit current depends on several factors such as the area of the PSC, the number of incident photons, the AM 1.5 standardized spectrum of the incident light, the absorption and reflection properties, and the collection probability. The short-circuit current density of the perfectly passivated surface can be approximated as:

$$J_{SC} = qG\ (L_n+L_p)$$

Where, G is the generation rate, and L_n and L_p are the electron and hole diffusion lengths, respectively. The short circuit current density is measured in mA/cm^2.

ii) Open-circuit voltage

The open circuit voltage (Voc) is the maximum available voltage from the perovskite solar cell at zero current and is defined as follows:

$$\text{Voc} = \frac{nkT}{q} In(\frac{I_L}{I_0} + 1)$$

From the above equation, it can be seen that Voc depends on the saturation current of the PSC and the light-generated current. The Voc is a measure of the amount of recombination in the device

iii) Fill Factor

Fill factor is defined as the ratio of the maximum power from the perovskite solar cell to the product of Voc and Isc and is defined as:

$$FF = \frac{P_{MP}}{V_{oc} \times I_{SC}}$$

$$FF = \frac{V_{MP} \times I_{MP}}{V_{oc} \times I_{SC}}$$

iv) Perovskite solar cell efficiency

The efficiency of PSC is defined as the ratio of energy output from the PSC to input efficiency from the sun and is defined as:

$$\eta = \frac{\text{Voc} \times \text{Isc} \times \text{FF}}{P_{in}}$$

Where, maximum power for PSC is defined as:

$$P_{max} = \text{Voc} \times \text{Isc} \times \text{FF}$$

Usually, the input power for efficiency calculation is 100mW/cm^2.

1.2. Perovskite solar cell structure

Device architectures

The first PSCs was developed from dye-sensitized solar cells (DSCs) in 2006, when $CH_3NH_3PbI_3$ was employed as the dye sensitizers in DSCs. PSCs structures are mainly divided into planar and mesoscopic structure.

i) Mesoporous structure

Initially, based on the pre-assumptions of DSCs, perovskite absorber was coated on the TiO_2 surface, where it undergoes photoexcitation by absorbing light of similar wavelength with its bandgap, and then excited electrons from the lowest unoccupied molecular orbital (LUMO) of the perovskite are injected into the conduction band (CB) of TiO_2 , which further transfer them to the FTO electrode. Later, the study with and without TiO_2 or Al_2O_3 layer revealed that the excitons can be transported through the perovskite film itself, semiconducting layer is no more essential, as it is required for the DSCs. Therefore, it differentiated the working of PSCs from the DSCs, and further research on the device architecture unfolded that PSCs working is more likely matches with solid state p-n junction solar cells. The schematic of mesoporous is illustrated in **Figure 1.2**.

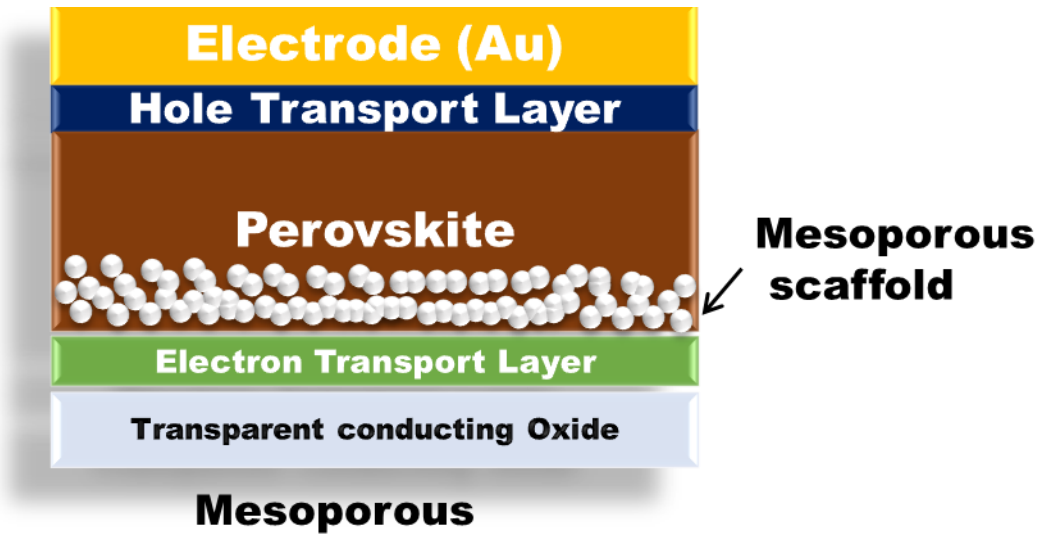

Figure 1.2. Schematic representation of mesoporous architecture in PSCs.

ii) Planner structure

As stated earlier, the working principle of PSCs closely matches to the solid state p-n junction solar cells, where the perovskite absorber has intrinsic properties. In planner perovskite structure, the absorber layer is sandwiched between p and n type layers, in either p-i-n or n-i-p configuration. The selection of specific p or n type materials depends upon the device configuration, energy levels of perovskite materials, and the electrical properties. In the n-i-p structure, the perovskite absorber is sandwiched between hole transporting layer (HTL) which works as p-type material and electron transporting layer (ETL) which works as n-type material. Where, the most commonly used ETL materials are TiO_2, SnO_2, while spiro-OMeTAD is the most widely used HTM. The n-i-p structure, which is usually known as conventional structure, follows ITO/TiO_2/perovskite/spiro-OMeTAD/Au configuration, where the HTL, ETL, and electrode materials are decided accordingly with energy level match. The configuration of n-i-p structure is shown schematically in **Figure 1.3a**.

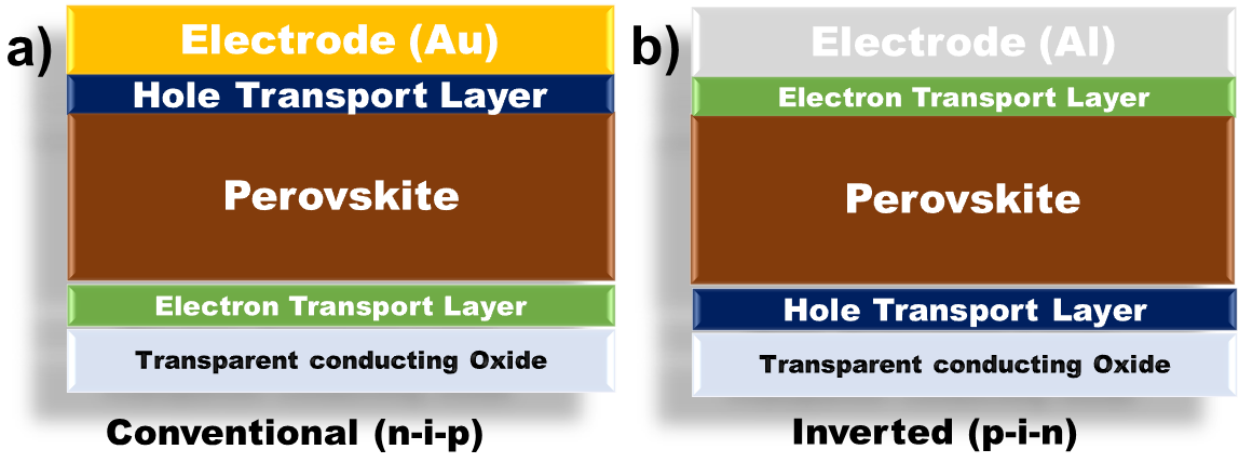

Figure 1.3. Schematic representation of PSCs architecture. a) Planar n-i-p structure, b) Planar p-i-n structure.

In p-i-n structure, usually termed as inverted structure, perovskite absorber is sandwiched between a p-type (for example, PTAA, PEDOT: PSS) HTL at the bottom and an n-type (for example, ITIC, PCBM) ETL at the top. The most commonly used inverted structure follows ITO/PEDOT: PSS/ Perovskite/PCBM/Al, where the perovskite layer absorbs the light and excitons are selectively separated by ETM and HTM layers. Therefore, the working mechanism of PSCs can be summarized as carrier generation, charge separation, and charge transport. However, the quasi Fermi levels at the contacts (i.e, between n-type and p-type layers) in both conventional and inverted structures limit the open circuit voltage.

1.3. Degradation mechanism of perovskite materials

Perovskite materials are prone to degradation when they are exposed to oxygen, heat, humidity, light and so on. For commercialization, the photovoltaic device should operate for more than 25 years in the outdoor conditions. For instance, the PSCs must qualify a set of standards in terms of stability, where the PSCs have to maintain minimum stability over 500 hours under 1 sun illumination and 1000 hours under full sunlight without encapsulation. Initially, it is important to understand the origin of degradation to improve the stability of the perovskite solar cells. For example, the well-established $MAPbI_3$ perovskite undergoes degradation via the following reactions.

$CH_3NH_3PbI_3(s) \leftrightarrow PbI_2(s) + CH_3NH_3I(aq)$

$CH_3NH_3I(aq) \leftrightarrow CH_3NH_2^+ + HI(aq)$

$4HI(aq) + O_2 \leftrightarrow I_2 + H_2O$

$2HI(aq) \leftrightarrow H_2 + I_2(s)$

Therefore, exposure to moisture leads is related to the degradation of $MAPbI_3$, which transforms it into MAI salt and metal halides, while the migration of metal halides can also promote PSCs degradation. Walsh and coworkers exhibited that once the $MaPbI_3$ is exposed to moisture, $CH_3NH_3PbI_3$ coordinates with H_2O to form an intermediate $[(CH_3NH_3^+)_{n-1}(CH_3NH_2)_nPbI_3][H_3O]$, eventually deteriorating the stability of the perovskite. Furthermore, the sources of perovskite degradation are illustrated by schematic diagram, as shown in **Figure 1.4.**

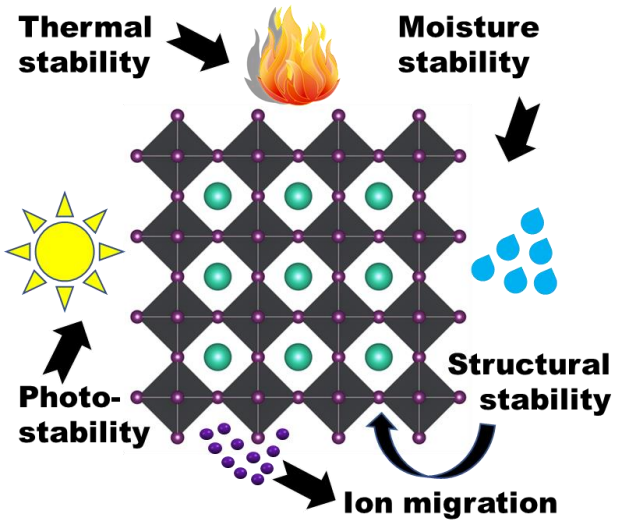

Figure 1.4. Schematic illustration of degradation sources for perovskite materials.

Additionally, grain boundaries are an important gateway for ion migration, where ions migrate through the contacts in the device, which instigates instabilities. It was reported that the

iodide anion migrates through the hole transport layer (HTL) towards the back-contact metal. In their studies, silver (Ag) and gold (Au) were studied, and it was found that ion migration form AgI and AuI under normal conditions, which degrades the perovskite material.

Moreover, the intrinsic thermal decomposition of perovskite materials remains ambiguous as the information provided by the thermogravimatric analysis (TGA) experiment provides only total mass-loss rates and percentages. Only a few information is available about the gaseous species released upon thermal degradation. Based on the earlier literature, there are two possible pathways for the thermal decomposition of $MaPbI_3$ (**Figure 1.4**), which are as follows

$CH_3NH_3PbI_3 \rightarrow CH_3NH_2+HI+PbI_2$

$CH_3NH_3PbI_3 \rightarrow NH_3+CH_3I+PbI_2$

It was concluded that the HI and CH_3NH_2 were released consecutively based on the weight loss percentage data from TGA. While another study suggested that the decomposition of $MaPbI_3$ is similar to methylammonium iodide (MAI), which decomposes into NH_3 and CH_3I.

Further, it was found that $FaPbI_3$ has better thermal stability than $MaPbI_3$ because FA cation has a stronger interaction with PbI_6 octahedra than of MA cations. Also, IHPs are expected to be more thermally stable compared to HHPs as inorganic cation decomposes at a higher temperature, but only limited studies related to thermal stability are reported so far on the thermal stability of IHPs.

1.4. Structural stability issues in perovskite materials

The stability of perovskite crystal ultimately depends on the tolerance factor (τ) and an octahedral factor (μ), as discussed above. When the value of τ lies between 0.81 and 1.11, it is believed to form a stable structure at room temperature. Additionally, when τ is between 0.9-1.0, it is expected to be ideal cubic perovskite, while any other smaller or higher value of τ are likely to forms distorted structures tetragonal, rhombohedral, hexagonal or orthorhombic. At present, the τ value for the most commonly used perovskite $CH_3NH_3PbI_3$ is 0.91, where the ionic radius of $CH_3NH_3^+$, PB^{2+}, and I^- is 0.18, 0.119, and 0.220 A°, respectively. However, τ can be adjusted by partial introduction or replacement of ions with different sizes to obtain a more stable perovskite structure. Usually, perovskite materials are categorized into two categories based on the nature of A-site cation, all inorganic and organic-inorganic perovskite materials.

All inorganic perovskite material consists of inorganic A-site cations such as Cs^+ and Rb^+. Furthermore, Pb^{2+} and Sn^{2+} are ideally suitable for B-site cation, while X-site can have halide materials such as Cl^-, Br^-, I^-. However, τ value suggests that $CsPbX_3$ and $CsSnX_3$ hold the cubic structure, where $CsPbI_3$ and $CsSnI_3$ have a tunable bandgap of 1.73 and 1.30 eV, respectively. Unfortunately, CsPbI3 has a low tolerance factor of ~0.80 and it has δ-phase at room temperature,

while it transforms to α-phase after annealing above ~330°C. Here, it is important to note that δ-phase is photo-inactive, while α-phase is photoactive. Furthermore, adding a smaller amount of hydroiodic acid to the precursor solution stabilizes the α-phase at low temperatures.

Similarly, Organic-Inorganic perovskite materials have organic cation at A-site cation such as MA ($CH_3NH_3^+$), FA (HC $(NH_2)_2^+$), GA (CH_5N_3), etc. However, HC $(NH_2)_2PbI_3$ exhibits photo-inactive β-phase at room temperature and FA^+ tends to decompose into ammonia. FA^+ has a larger ionic radius of 0.253 nm than MA^+ 0.217 nm, respectively, which results in the expanded crystal lattice. Eventually, the Pb-I bond distance decreases, which lowers the bandgap. The black phase-stabilized $FAPbI_3$ shows a bandgap (Eg) of 1.47 eV, while $MaPbI_3$ has a bandgap of 1.55 eV. Although, $FaPbI_3$ is supposed to be more efficient than $MaPbI_3$ because of its extended absorption edge, and the solar cell devices show higher (JSC) due to its lower bandgap.

Additionally, to overcome the structural instability of $FaPbI_3$, a partial replacement of MA with FA with a composition of 20 mol% stabilizes the trigonal α-$FaPbI_3$ at room temperature. It has been reported that, when a Ma^+, which has a 10 fold higher dipole moment than FA^+, is partially preplaced, it stabilizes the 3D arrangement of α-$FaPbI_3$ with slight lattice shrinkage. It was proposed that partial incorporation of MA^+ exhibits stronger interaction with the PbI_6^{4-} octahedral. Moreover, the thermal stability of $MaPbI_3$ is lower than Ma incorporated $Ma_xPb_{1-x}PbI_3$, as the thin films decompose back to the orthorhombic phase after annealing above 150 °C. While, the $Ma_xPb_{1-x}PbI_3$ thin films maintain the black phase at similar temperatures, it was proposed that FA has a stronger interaction with PbI_6^{4-} octahedral and has higher probability to form hydrogen bonding. Therefore, structural and thermal stability are related with increased tolerance factor and a stronger interaction of FA with PbI_6^{4-} octahedral.

Apart from this, cesium (Cs) cation was incorporated with a composition of 15 mol% in $FaPbI_3$ to achieve more stable trigonal α-$FaPbI_3$ phase. The τ value of $FA_{0.85}Cs_{0.15}PbI_3$ was found to be 0.9 and it forms a stable cubic phase. The absorbance value of $FA_{0.85}Cs_{0.15}PbI_3$ was found to be higher than $FAPbI_3$, when both films were exposed to humidity for 18 days; the absorbance value of $FA_{0.85}Cs_{0.15}PbI_3$ remained constant while that of $FAPbI_3$ decreased very rapidly. Moreover, it was found that Cs/FA mixture perovskite films enhanced the thermal and humidity stability of PSCs.

Apart from A-site cation, B-site metal cation in ABX_3 is also important for the structural stability of the perovskite materials. The most commonly used Pb atom is toxic and it faces a potential barrier to commercialization. So, it is important to find a suitable non-toxic or environment friendly alternative. While, it has been reported that partial substitution of Sn^{2+} with Pb^{2+} decreases the stability of the crystal lattice, because of its lower inert pair effect. Also, Sn^{2+} easily oxidizes to Sn^{4+} which is detrimental for the structural stability of the perovskite. Furthermore, Sn^{2+} based perovskite exhibit broad absorbance and covers up to infrared region; also they have higher thermal and photo

stability. Therefore, we need fundamental study on the stability and performance of lead free perovskite solar cells.

1.5. **Grain boundary defects** in perovskite solar cells

Addressing the surface and grain boundary passivation in perovskite thin films plays a vital role in improving the PSC's performance as well as stability. Grain boundary defects are one of the prevalent surface defects which hinder the electrical and thermal properties of the perovskite materials. Crystal grain boundaries and bulk point defects are responsible for ion migration. During the thermal annealing process, partial organic species might evaporate from the grain boundaries that leave the open space at grain boundaries. This ion migration leads to perovskite degradation but it is still unclear about the winner among the halide ions and organic compounds. Though, several efforts have been done for the passivation of grain boundaries, including alkylammonium post-treatment, wide bandgap halides coating, secondary amines incorporation, and capping ligands coating, etc. The post-treatment with long-chain alkylammonium improved the device performance but their function for stability improvement is not significant. Secondary or tertiary amines will be the more "static" solution for defect passivation as well as enhancement in moisture resistance, and thus more research will be focused on addressing the surface interaction between intermediate layers.

1.6. **Progress in moisture stability**

The coating of perovskite layers with metal oxides, polymers, metal hydroxides, MOFs, aromatic amines, etc. was used exhaustively but many of them failed to provide full encapsulation and device performance improved insignificantly. Recently, 2D/3D interfaced bilayers of perovskite were explored in solar cells, but they failed to reach the prior established device performances. Although it offers high stability and better charge separation, the bandgap increases as the number of 2D layers increases which limit the device performance. Furthermore, metal hydroxides coating stabilized the perovskite in water, but this approach is still in the infancy stage, and thin-film processing must be addressed for the high-performance device. However, the thickness of the dielectric layer coating on perovskite material is still mysterious and it needs further investigation as it may have dexterous effects on the electrical properties of the active layer. The other alternatives used so far improved the stability several folds but they are not been able to abolish the stability issue. Interestingly, recent trends show that secondary, tertiary, and high bandgap halides have the potential to stabilize the α-phase of $FaPbI_3$ perovskite without compromising the bandgap.

Chapter 2

A thermally stable, barium stabilized α-$CsPbI_3$ perovskite for optoelectronic devices

2.1. Abstract

All inorganic perovskite, $CsPbI_3$ has emerged as an alternative photovoltaic material due to its non-volatile composition and promising photovoltaic performance comparable to organic-inorganic hybrid perovskite. However, spontaneous deformation from light-active black phase to light-inactive yellow phase under ambient condition, poor air stability, low thermal stability as well as high-temperature processing are challenging issues in fabricating $CsPbI_3$-based solar cells. Herein, we introduce a new surface passivation strategy using camphor sulfonic acid (CSA) to improve surface morphology and air stability for the Ba-stabilized α-$CsPbI_3$ perovskite at low temperature. The surface passivated, Ba-doped α-$CsPbI_3$ is thermally stable upon annealing as well as highly photo-stable over a year, and it also exhibits ~1.72 eV band gap suitable for optoelectronic applications. All inorganic solar cells based on the Ba-doped α-$CsPbI_3$ retain 98% of its initial PCE values even after 700 hours, also the red light-emitting diodes (LED) exhibit the light emission at 700 nm with bandwidth 39 nm. This is the first study for surface passivated, Ba-stabilized α-$CsPbI_3$, which provides opportunities for new developments of highly efficient tandem solar cells and other optoelectronic devices.

2.2. Introduction

In the pursuit of low cost and easy fabrication of solar cells, perovskite has emerged as a strong candidate for the future energy material. Organic-inorganic hybrid halide perovskite solar cells have recorded the efficiency over 20%[1–3] by optimizing thin-film growth, interface, and absorber materials. However, the volatile nature of organic cations (i.e., methylammonium (MA^+) and formamidinium (FA^+)) in ABX_3 crystal-structured perovskite (A = Cation, B = Metal anion, X = halide) hinders its stability under environmental stresses such as moisture, heat, oxygen, and ultraviolet (UV) light. Moreover, alternating routes have been explored to resolve the stability issue. Cations such as cesium (Cs^+) and rubidium (Rb^+) have been mixed with the existing cations (MA^+, FA^+) to obtain good properties, but still the thermal stability is a serious issue. Non-volatile and hysteresis-free characteristics of inorganic perovskite materials attracted attention in recent years after several reports on a low-temperature α-phase stabilization of $CsPbI_3$.[4–9] One-step solution processing offers ease of fabrication, while high photo-stability benefits long-term stability. Cesium lead iodide perovskite solar cells emerge as a new alternative for stable perovskite solar cells and have achieved the efficiency from 2.9 upto 17.06% within a small span of time.[6,10–13] Unfortunately, it suffers from the metastable phase at room temperature. Thin films when heated above 330°C exhibits α-phase black

perovskite, while upon cooling down to room temperature it changes back to its original orthorhombic δ-phase.[13,14] The incorporation of cesium cation leads to phase transition because it is too small to fit inside $[PbI_6]^{4-}$ octahedra in the cubic perovskite structure.[10,14,15] Snaith et al. reported black phase stabilization of cesium lead iodide perovskite at room temperature using hydroiodic acid (HI) showing a PCE of 2.9%.[13] The microstrain induced in the crystal lattice by HI was believed to be the major reason for the α-phase stabilization at room temperature. After that, there were several reports on stabilizing the α-phase by employing excess HI with additional additives, but it still lacks thermal and air stability.[16–18] On the other hand, partial substitution of the I^- site with smaller Br^- stabilized the black phase and improved the thermal stability of the inorganic perovskite with a remarkable PCE of 13.74% but it resulted in an increased band gap up to 1.92 eV[8,19–21]. Recently, the construction of black phase of perovskite was extended to different partial doping of metal ions into B site metal such as bismuth, tin, europium, strontium, and calcium with an average PCE of around 13% or less.[22–25] However, in most of these reports, air stability, surface morphology, and doping concentration optimization are serious issues. The α-$CsPbI_3$ perovskite exhibits a suitable band gap of 1.73 eV for solar cells application.[4,26] Stabilizing α-phase of $CsPbI_3$ perovskite at room temperature will open a new window for high efficiency and easy processing of perovskite solar cells. Zhao et al. reported an inspiring record of 17.06% efficiency with low-temperature processed α-$CsPbI_3$ perovskite.[4] Although the PCE of these solar cells is approaching towards the values of organic-inorganic perovskite counterparts, the air instability, high-temperature processing and thermal instability are still challenging issues with the α-phase of $CsPbI_3$.

The solubility of $CsPbI_3$ is poor even in polar solvents like DMSO and DMF.[27] Introducing a small amount of HI or incorporating a small amount of sulfonic acids increases the solubility and also stabilizes the black phase at room temperature.[13,16] The crystal grain size of these α-$CsPbI_3$ thin films reduces to ~100 nm and these thin films are not thermally stable as it turns back to yellow phase after annealing at ~100°C. Also, these films suffer from large pin holes which limit the charge transport mechanism.[28] Partial substitution of iodide with bromide to form $CsPbI_2Br$ or $CsPbIBr_2$, or $CsPbBr_3$ can solve this issue, but it increases the band gap towards ~1.92 eV,[8,29] which is not favorable for solar cells application. Stabilizing the α-phase of $CsPbI_3$ perovskite at low temperature and obtaining thermally stable black phase films will open new opportunities for red LEDs, solar cells, photo-detectors, and other optoelectronic devices.

To solve the phase, thermal, and air stability issues associated with α-$CsPbI_3$, we studied the incorporation of surface passivation and B-site doping simultaneously. Here, for the first time, we integrated CSA additive and Ba-doping for surface passivation and α-phase stabilization of $CsPbI_3$ perovskite. We observed that the CSA incorporation improved air stability as well as the surface morphology, while the partial replacement of Ba^{2+} with Pb^{2+} stabilized the α-phase of $CsPbI_3$ at low

temperature. Also, Ba-doping led to the higher thermal stability of perovskite (i.e., Ba has a higher melting point of 727 °C than Pb of 327 °C). In this study, our density functional theory (DFT) calculations predicted the optimal Ba-doping amount from the variation of formation energy at different doping levels. Finally, we applied the α-$CsPbI_3$ perovskite for solar cells and light-emitting diodes devices. We fabricated one-step solution processed inorganic PSCs and red LEDs at low temperature. The Ba-doped perovskite thin films showed higher phase stability upon annealing than HI- or CSA-stabilized α-$CsPbI_3$ thin films and maintained black phase even after annealing up to 300°C as shown in **Figure 2.1** a-c. The typical planar PSCs were fabricated with the configuration of ITO/SnO_2/perovskite/poly (3-hexylthiophene-2,5diyl)(P3HT)/Au having different concentration of CSA in $CsPb_{0.90}Ba_{0.10}I_3$ precursor solution. The 2, 5, and 10 wt% of CSA in $CsPb_{0.90}Ba_{0.10}I_3$ perovskite solutions are denoted as CSA-1, CSA-2, and CSA-3, respectively. The CSA-2 PSCs exhibited a PCE of 7.23%. Red LEDs fabricated with CSA-2 perovskite in ITO/Poly(3,4-ethylenedioxythiophene): poly (styrenesulfonate) (PEDOT : PSS) / perovskite / 2,2',2''-(1,3,5-Benzinetriyl)-tris(1-phenyl-1-H-benzimidazole) (TPBi) / LiF / Al exhibited a characteristic deep red emission at 700 nm with maximum brightness of 2.17 cd m^{-2}, external quantum efficiency (EQE) 0.04%, and full width at half maximum (FWHM) 39 nm. This is the first low-temperature processed inorganic PSCs and red LEDs with Ba-stabilized α-$CsPbI_3$ perovskite having excellent thermal stability. By optimizing the charge transport interlayers, the efficiency of the red LEDs and solar cells can be improved further.

2.3. Experimental Section

2.3.1. Chemicals

Barium Iodide (BaI_2, 99.9%), (1S)-(+)-10-camphor sulfonic acid (CSA, 99%), cesium iodide (CsI,99.9%), lead iodide (PbI_2,99.9%), dimethyl sulfoxide (DMSO, anhydrous, 99.8%), poly(3-hexylthiophene-2,5-diyl) (P3HT, with 85000-10000 wt), chlorobenzene (CB, anhydrous 99.8%) and all other chemicals including N,N-dimethylformamide (DMF, anhydrous, 99.8%) were purchased from Sigma-Aldrich. All salts and solvents were used as received without any further purification.

2.3.2. Inorganic Perovskite Precursor Solution Preparation

The $CsPbI_3$ precursor solution was prepared by dissolving CsI and PbI_2 (1 : 1 mmol) with a mixture of DMSO and DMF (4 : 6, v : v) as solvent. The Ba^{2+} incorporated $CsPbI_3$ perovskite precursor solution was prepared by dissolving 0.01 mol CsI and 0.01 mol (90/10 mol %) mixture of PbI_2/BaI_2 and CSA (2, 5, and 10 wt% of $CsPb_{1-x}Ba_xI_3$) in 1 ml of solvent with DMSO and DMF mixed (4: 6, v : v). The final solution was stirred for 2 h at room temperature. The HTL solution was prepared by dissolving P3HT (10 mg) in 1 mL chlorobenzene and adding 10 μL of (4F-TCNQ-Sigma-Aldrich) in chlorobenzene (1mg/1ml).

2.3.3. Solar Cells Fabrication

Firstly, Indium tin oxide (ITO) conducting glass was ultrasonically cleaned by detergent, deionized water, acetone and isopropyl alcohol for 15 min each and then treated by a UV/O_3 cleaner for 30 minutes. Then, a compact ~20 nm thin SnO_2 layer was spin-coated on the glass/ITO substrates followed by annealing at 150°C for 15 minutes. After depositing the electron transport layer, the perovskite layer was deposited by one step spin-coating method using the 1 mM $CsPbI_3$ precursor solution at the speed of 3000 rpm for 30 s followed by annealing at 60°C for 1 minute and then at 120°C for 10 minutes. Then, an HTL layer of P3HT was spin-coated at 3000 rpm for 30 s with a ramp rate of 1000 rpm/s. Finally, 80 nm thick gold electrode as the top electrode was deposited through the shadow mask using thermal evaporation with an active area of 0.130 cm^2.

2.3.4. Characterization and measurements

A digital source meter (Keithley 2635A) was used to measure current density–voltage (*J–V*) characteristics of the solar cells. Solar cells performance was measured under illumination by an Air Mass 1.5 Global (AM 1.5 G) solar simulator with an irradiation intensity of 100 mW cm^{-2}. Apertures (13.0 mm^2) made of thin metal were attached to each cell before measurement for *J–V* characteristics. The device stability was measured in time step. EQE measurements were obtained with a PV measurements QE system under ambient conditions, with monochromated light from a xenon arc lamp. The monochromatic light intensity was calibrated with a Si photodiode and chopped at 100 Hz. The absorption properties of thin film were characterized by UV-Vis-NIR (Carry 5000, Agilent) while thin film PL was measured with fluorometer (Carry Eclipse, Agilent) excited at 450 nm. The surface morphologies of perovskite with/without additive were analyzed by field emission SEM (Nova NanoSEM, FEI). We collected the fourier-transform infrared (FTIR) spectra of the thin films using FTIR (670-IR, Varian). The crystallographic information was determined by high power XRD (MAX 2500V, Rigaku) using Cu Kα radiation (λ = 1.54059 Å) with scanning angle 2θ ranging from 10° and 60°. Chemical composition of the samples were investigated by XPS (K-alpha, ThermoFisher), while elemental composition distribution measurements were carried out in depth profiling mode using TOF SIMS 5 (ION TOF) and the thickness of the samples were measured by surface profiler (KLA Tencor).

2.3.5. Light-Emitting Diodes fabrication

The ITO substrates were cleaned from the above mentioned method and treated by a UV/O_3 cleaner for 30 minutes. A poly(3,4-ethylenedioxythiophene) : polystyrene sulfonic acid (PEDOT : PSS) layer was deposited on cleaned ITO substrates by spin-coating at 4000 rpm for 40 s, followed by annealing at 150 °C for 15 min. On top of the PEDOT : PSS layer, the perovskite layer of CSA-2 in 1 : 1 molar ratio was spin-coated at 4000 rpm and annealed at 100°C for 10 minutes. The 100 nm thick TPBi

layer was deposited through the shadow mask using thermal evaporation with an active area of 0.130 cm^2. Finally, a 100 nm thick Al layer was deposited under vacuum (< 106 Torr) using thermal evaporation.

2.3.6. Density functional theory calculations

We performed DFT calculations using PBE exchange correlation functional[33] and Tkatchenko−Scheffler (TS)[34] van der Waals corrections in conjunction with PAW planewave basis sets of 500 eV energy cut-off in (2×2×2) G-centered k-point mesh for the (3×3×3) supercell of cubic $CsPbI_3$ using VASP suite.

2.4. Result and Discussion

To overcome the air and thermal stability issue, we introduced 2, 5, and 10 wt% of CSA in $CsPb_{0.90}Ba_{0.10}I_3$ precursor solution and studied their effects on α-phase stability, crystal growth, air stability, thermal stability, and optical properties of $CsPbI_3$ perovskite. The thin films were stable enough in humid conditions without encapsulation to record the absorption, PL, and lifetime data, whereas in earlier reports, encapsulation was used to characterize those properties. We also noticed that the simultaneous substitution of CSA and Ba (10 mol %) in $[PbI_6]^{4-}$ octahedra does not affect the absorption and emission properties significantly, with a bandgap of ~1.72 eV, similar to that of α-$CsPbI_3$.[26] Moreover, this is the first report for the partial replacement of B-site cation without any access HI or Br^- to stabilize α-$CsPbI_3$. The schematic illustration in **Figure 2.1(a-c)** represents the effect on thin film characteristics observed during processing the films at different temperatures.

2.4.1. DFT calculations

To elucidate the origin of stability effect of BaI doping to α-$CsPbI_3$, we calculated the formation energy of α-$CsPb_xBa_{(1-x)}I_3$, $E_f = E(\mathrm{CsPb_{(1-x)}Ba_xI_3}) - xE(\mathrm{CsBaI_3}) - (1-x)E(\mathrm{CsPbI_3})$ using DFT by varying the BaI doping ratio x = 3.7, 7.4, 11.1, 14.8, 22.2 % *etc*. We find that E_f for α-$CsPb_xBa_{(1-x)}I_3$ has the minimum at x = 11.1 % **(Figure 2.1d)**, which is similar to the experimental BaI doping rate of 10 %.

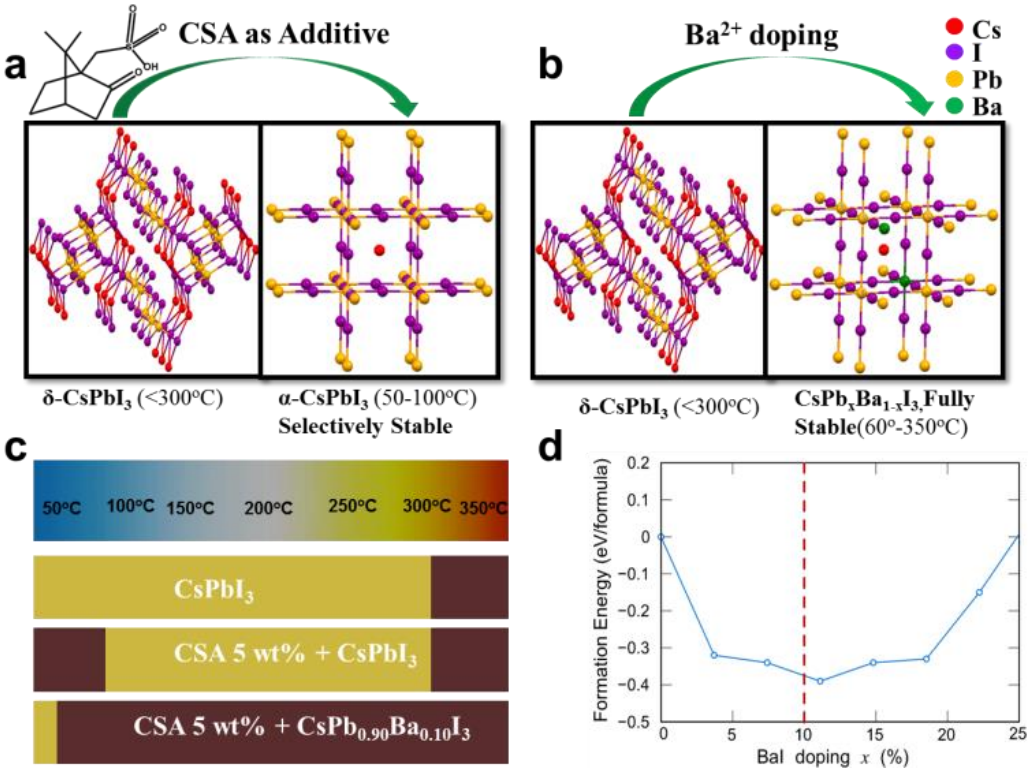

Figure 2.1. a,b) Schematic representation of phase stabilization with CSA additive scheme (left) and Ba-doping scheme (right) with comparative description of their $CsPbI_3$ properties. c) Schematic representation of the phase change in $CsPbI_3$ thin films observed at different temperatures. Yellow and browm colors represent the δ and α-phase of $CsPbI_3$. δ-$CsPbI_3$ changes to α-$CsPbI_3$ after annealing above ~330 °C, CSA 5 wt% stablize the α-phase of $CsPbI_3$ between 50-100 °C and transform back to δ-$CsPbI_3$ above 100°C, while CSA and Ba-doped films are stable in α-phase between 60-350 °C. d) The formation energy E_f(eV/formula) of a-$CsPb_xBa_{(1-x)}I_3$ with respect to the BaI doping rate x = 3.7, 7.4, 11.1, 14.8, 22.2 %. The red dashed line indicates the experimental BaI 10 % doping, consistent with the DFT-predicted optimal value.

2.4.2. Optical and Structural analysis

Experimentally, we found that the access HI accelerated the crystallization process and the thin films turned back to yellow phase if annealed above 100°C, and the partial substitution of Br^- in $CsPbI_3$ perovskite decreased the absorption range towards UV-region which directly limited the efficiency of the PSCs. **Figure 2.2a** shows that the orthorhombic $CsPbI_3$ film processed at low-temperature exhibited visible-light absorption below 450 nm, while samples CSA-1, CSA-2, and CSA-3 absorbed light up to ~720 nm wavelength and showed solid state photoluminescence (PL) spectra (**Figure 2.2b**). Also, the influence on crystal size and thin film morphology with varying concentration of CSA and δ-$CsPbI_3$ processed at low temperature was analyzed from field emission scanning electron microscope (FESEM) top images **(Figure 2.2c)**. The reference $CsPbI_3$ thin film had inhomogeneous

submicrometer-sized crystals with large sized pinholes, while the CSA (1-3) rearranged the crystal grains size ranging ~100- 150 nm without any pinholes. α-$CsPbI_3$ PSCs suffered from pin

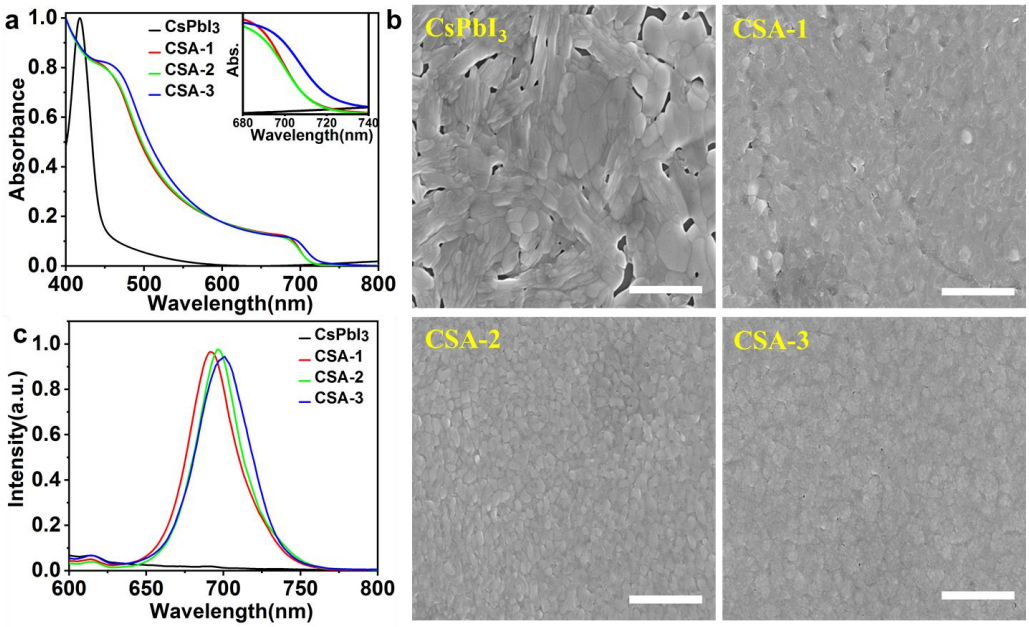

Figure 2.2. Optical spectra and surface morphology of $CsPbI_3$, CSA-1, CSA-2, CSA-3 films processed at low temperature. a) UV-vis absorbance spectra with or without CSA schemes. b) Solid state photoluminescence (PL) spectra of the films. c) Top-view FE-SEM images showing changes in crystal size and mitigation of pin holes with different schemes, scale bar: 1μm.

holes,[16,22–24,26] while we obtained pinhole-free thin films using CSA-2. This CSA-1 films were well crystallized, but sufferd from insignificant pinholes, while sample CSA-3 possessed undesired precipitation and inconsiderable pinholes. The phase and photo stability of thin films were observed for δ-$CsPbI_3$, CSA stablized $CsPbI_3$ and CSA-2 for over a year inside glove box, as shown in **Figure 2.3.** The CSA-2 thin films maintained their α-phase, while only CSA stablized thin films transformed back to δ-phase.

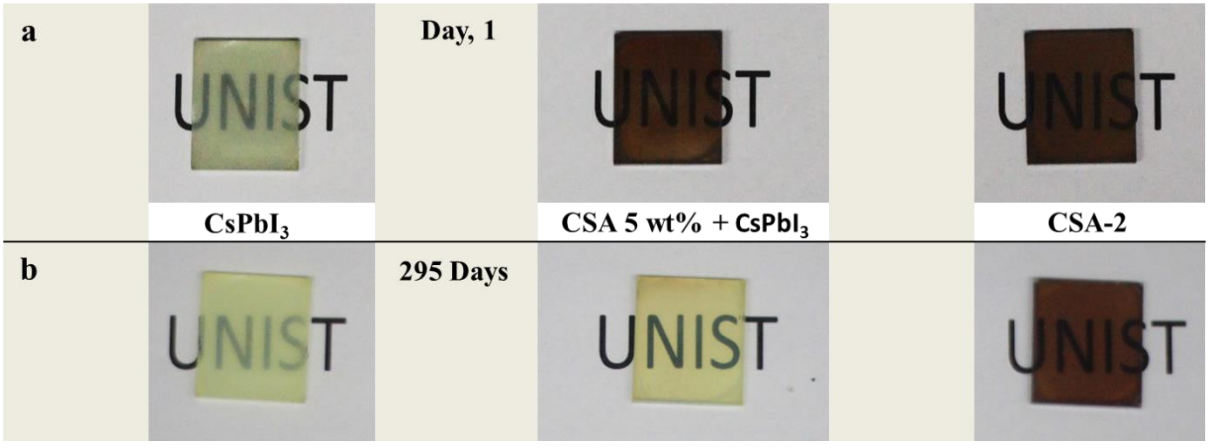

Figure 2.3. The photographs of inorganic perovskite processed at low temperature with a composition of pristine $CsPbI_3$, (CSA 5 wt% +$CsPbI_3$), and (CSA 5 wt% + $CsPb_{1-x}Ba_xI_3$). a) Day-1 photograph of the thin films stored inside the nitrogen glove box. b) Day-295 photograph of the thin films stored.

2.4.3. X-ray photoelectron spectroscopy

In order to study the influence of CSA incorporation and the effect of Ba-doping on the elemental composition at the surface of $CsPbI_3$ perovskite structure, X-ray photoelectron spectroscopy (XPS) was performed.[6,13,29,32,33] The Ba $3d_{5/2}$ and Ba $3d_{3/2}$ characteristic peaks at 780 and 795 eV, respectively indicate the successful incorporation of Ba^{2+} inside the structure, and the increment in CSA concentration resulted in the decrease of elemental peak intensities as shown in **Figure 2.4d**. We found that the CSA (1-3) films have only two characteristic peaks for Cs 3d, I 3d, Pb 4f and Ba 3d without any additional peaks; this indicates the absence of mixed phase inside the crystal lattice. However, split peaks were present with the two characteristic peaks in previous reports of α-$CsPbI_3$ films, which indicate the mixed phase inside the crystal lattice.[25,34] The presence of lower binding energy doublets in δ-$CsPbI_3$ XPS spectra indicates the non-interacted Cs^0, I^0, and Pb^0 reduced states and the non-perovskite phase.[25] The $CsPbI_3$ films processed at low temperature have Cs $3d_{5/2}$ and Cs $3d_{3/2}$ peaks at 723.9 and 738 eV, respectively, while the two additional peaks are observed at 726 and 740 eV (**Figure 2.4e**). Also, the δ-$CsPbI_3$ XPS spectrum shows four I 3d characteristics peaks at 618.2, 621.1, 629.7 and 632.6 eV (**Figure 2.4f**), which indicate the reduction of Cs^+ cation by the I^- anion inside the structure, and this causes deformation of the cubic symmetry.[35]

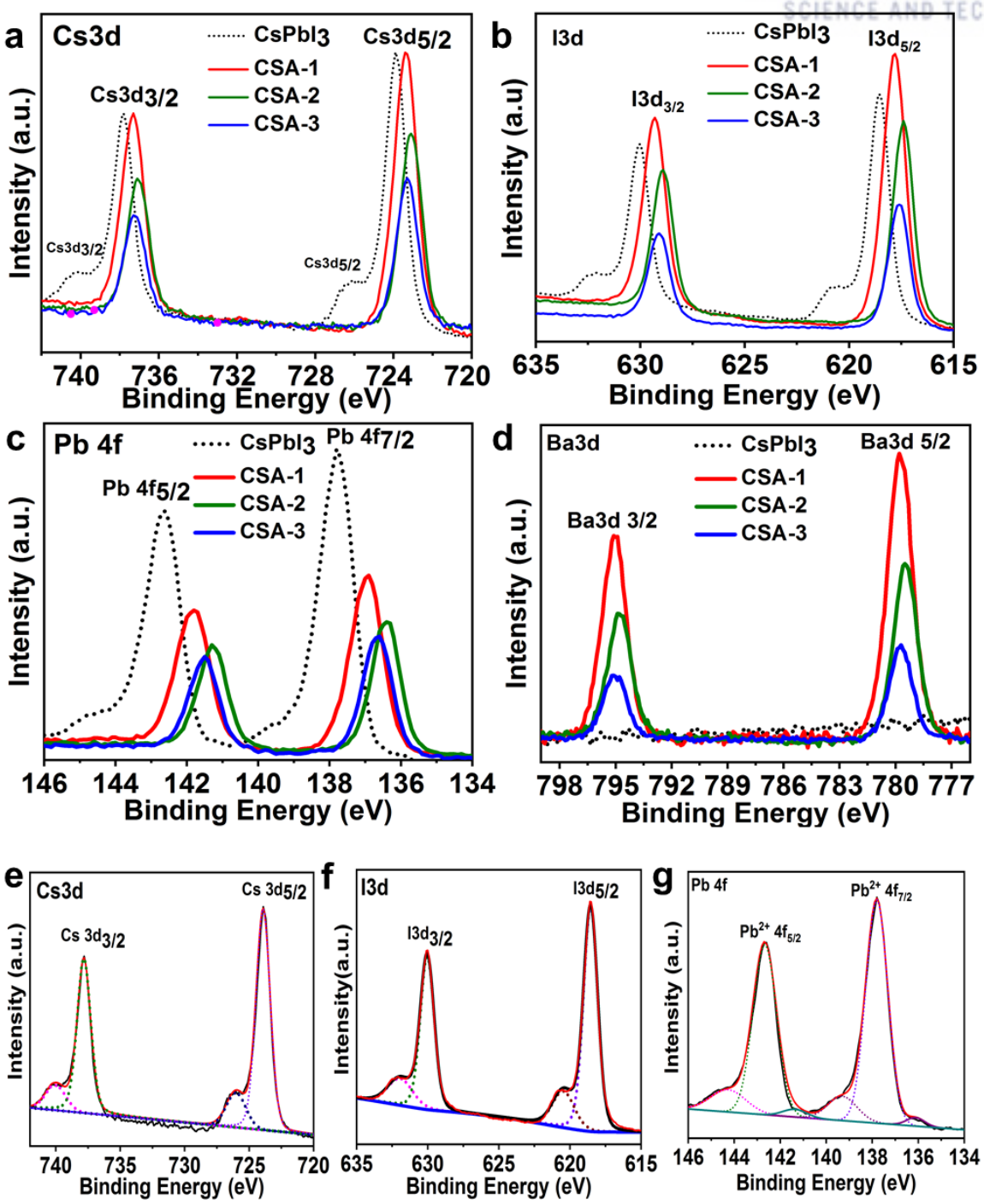

Figure 2.4. XPS spectra (a-d) of low temperature processed $CsPbI_3$ and CSA (1-3) schemes for a) Cs 3d, b) I 3d, c) Pb 4f, and d) Ba 3d [$CsPbI_3$ peaks are shown as dots, while CSA (1-3) schemes shown as solid lines]. Fitted results (e-g) of the low-temperature processed $CsPbI_3$ for e) Cs 3d, f)I 3d, and g) Pb 4f.

The δ-$CsPbI_3$ has two peaks of Pb^{4+} $4f_{7/2}$ and Pb^{4+} $4f_{5/2}$ at 139.3 and 144.2 eV,[35] respectively, two signature peaks of Pb^{2+} $4f_{7/2}$ and Pb^{2+} $4f_{5/2}$ at 137.8 and 142.6 eV, respectively, and also Pb^{0} $4f_{7/2}$ and

Pb^0 $4f_{5/2}$ peaks at 136.1 and 141.3 eV, respectively, which indicate the existence of different oxidation states of Pb inside the deformed crystal structure (**Figure 2.4g**).[13] The side peaks disappear from Cs 3d, I 3d, Pb 4f spectrum of CSA (1-3) films and also the binding energy peaks shift towards lower energies which indicate the orthorhombic to cubic phase transformation (**Figure 2.4a-c**).[25,35] On the other hand, the CSA (1-3) incorporated films have only two signature peaks of Pb^{2+} $4f_{7/2}$ and Pb^{2+} $4f_{5/2}$ at 136.9 and 141.8 eV, respectively, which indicate the cubic phase of the crystal lattice without any presence of orthorhombic phase. Similarly, the binding energy of Cs $3d_{5/2}$ and Cs $3d_{3/2}$ shift to 0.60 eV towards the lower energies, but there are no side peaks in all the CSA (1-3) films, which indicate no obvious reduction or break of cubic symmetry. The same phenomena of binding energy shifts are also observed in I 3d and Pb 4f spectra, which indicate the partial substitution of Ba inside the crystal lattice.

2.3.4. The nuclear magnetic resonance spectroscopy

The nuclear magnetic resonance (NMR) spectroscopy measurement was conducted to identify the interaction and potential mechanism for CSA-stabilizing α-$CsPbI_3$ (**Figure 2.5**).[26,36] We compared the precursor perovskite solution with pure CSA dissolved in DMSO-d_6 solution.

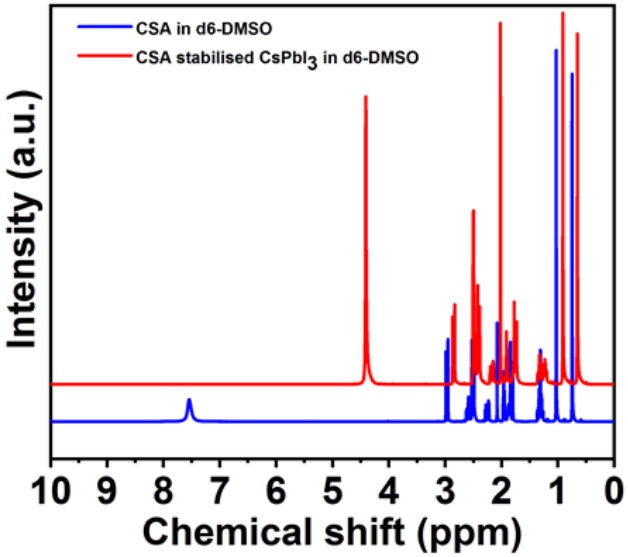

Figure 2.5. The NMR data representing the interaction of CSA with $CsPbI_3$, the characterization was done by dissolving the precursor solution in d-6 DMSO solution.

The pure CSA has a peak at δ = 4.39 ppm, and it shifts to downfield by Δδ = 3.11 ppm at δ = 7.5 ppm after interaction with the $CsPbI_3$ precursor, indicating that the -SO_3H group has strong interaction with $CsPbI_3$. Practically, we observed that the CSA (1-3) films are more resistant to moisture than $CsPb_{1-x}Ba_xI_3$ films. This persuades us to carry out the optimization of CSA concentration inside the inorganic perovskite precursor solution.

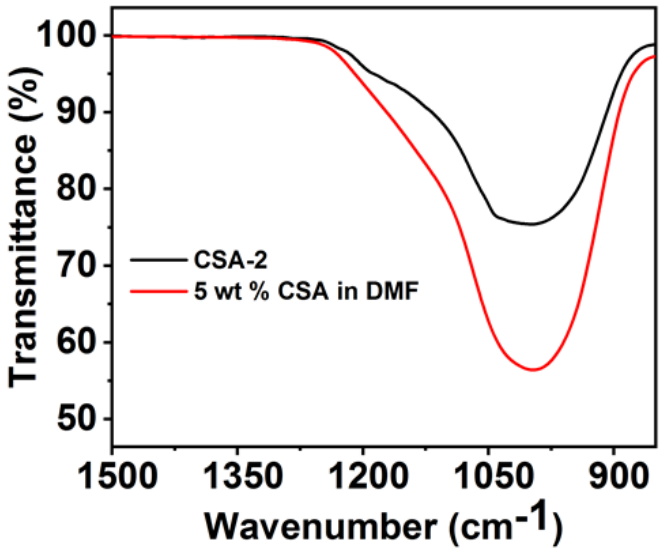

Figure 2.6. FTIR measurement of 5 wt % CSA and CSA-2 thin films.

The in-depth dynamics of the resistant to moisture was verified with the help of SEM, NMR, XPS, and Fourier transform infrared spectroscopy (FTIR) studies. Camphor sulphonic acid (CSA) strongly interacts with $CsPbI_3$ in both solution and solid-state as confirmed from SEM, NMR, XPS, and FTIR measurements **(Figure 2.6)**. CSA slows down the crystallization process of $CsPbI_3$ to grow small-grained $CsPbI_3$ films as observed in SEM images **(Figure 2.2c)**. In the absence of CSA, the sizes of $CsPbI_3$ grains are much larger. In XPS, we observed the peak shifts towards lower energy both in Pb $4f_{5/2}$ and Pb $4f_{7/2}$ peak positions which indicate the strong interaction of CSA with $CsPb_{0.90}Ba_{0.10}I_3$ thin films. From NMR, we confirmed that CSA strongly interacts with $CsPbI_3$. We have also performed FTIR to confirm the interaction of CSA with $CsPbI_3$ in solid-state thin films. The FTIR peak around 995 cm^{-1} corresponds to the symmetric S=O stretches of the sulphonate group (SO_3^-). In CSA incorporated $CsPbI_3$ thin films, the peak shifted to the higher wavenumber 1005 cm^{-1} which indicates the strong interaction of oxygen element of SO_3^- and $CsPbI_3$.[16] CSA has two S=O and one S-OH and the S–OH group loses its H^+ ion in solution to form S-O^-. The lone pair of oxide ion can participate in resonance and the S=O bond will get weaken. However, as SO_3^- interacts with $CsPbI_3$, the resonance is inhibited, and the S=O bond strength increases. CSA is an organosulphur bridge compound and one of the bridgehead carbon atoms contains two methyl groups. The head part of CSA i.e. SO_3^- interacts with the perovskite moiety and the tail part i.e. hydrophobic alkyl part resists the moisture. Thus, CSA makes a strong barrier for moisture, improving the air stability of $CsPbI_3$ thin films.

2.4.5. Structural and solar cells device analysis

The effect of Ba-doping and CSA concentration on crystal structure was characterized by using the high power X-ray diffraction (HPXRD) as s hown in **Figure 2.7, 2.8a**.

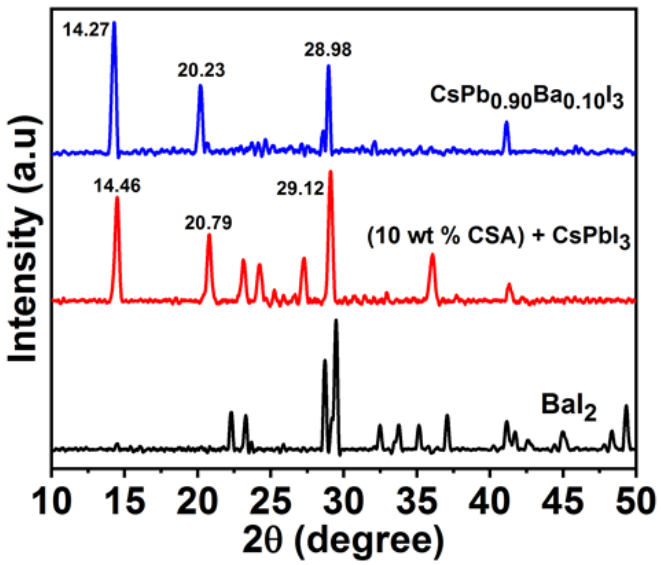

Figure 2.7. XRD pattern of the BaI_2, CSA stabilized $CsPbI_3$, and Ba doped $CsPbI_3$ thin films.

We observed characteristic peaks at 14.46°, 20.79° and 29.12° in CSA stabilized $CsPbI_3$ **(Figure 2.9)**, while Ba^{2+} doped thin films have characteristic peaks at 14.27°, 20.23° and 28.98°, which indicates the peak shift towards the lower θ value. The shift in XRD peaks towards lower θ value indicates the replacement of smaller cation (Pb^{2+} with ionic radius 119 pm) with the larger cation (Ba^{2+} with ionic radius 135 pm). Also, BaI_2 XRD peaks were absent in Ba^{2+} doped $CsPbI_3$, which indicates the complete incorporation of Ba^{2+} cation inside the perovskite structure. Previously, the lattice strain induced by excess HI stabilized the cubic phase, and the grain size was reduced significantly to ~100 nm, which was small compared to the submicrometer-sized grain of the films processed without HI.[4,6,13,16,37,38] In this case, lower ionization energy and strong lattice strain induced by CSA and Ba-doping stabilized the cubic phase of $CsPbI_3$ at low temperature.

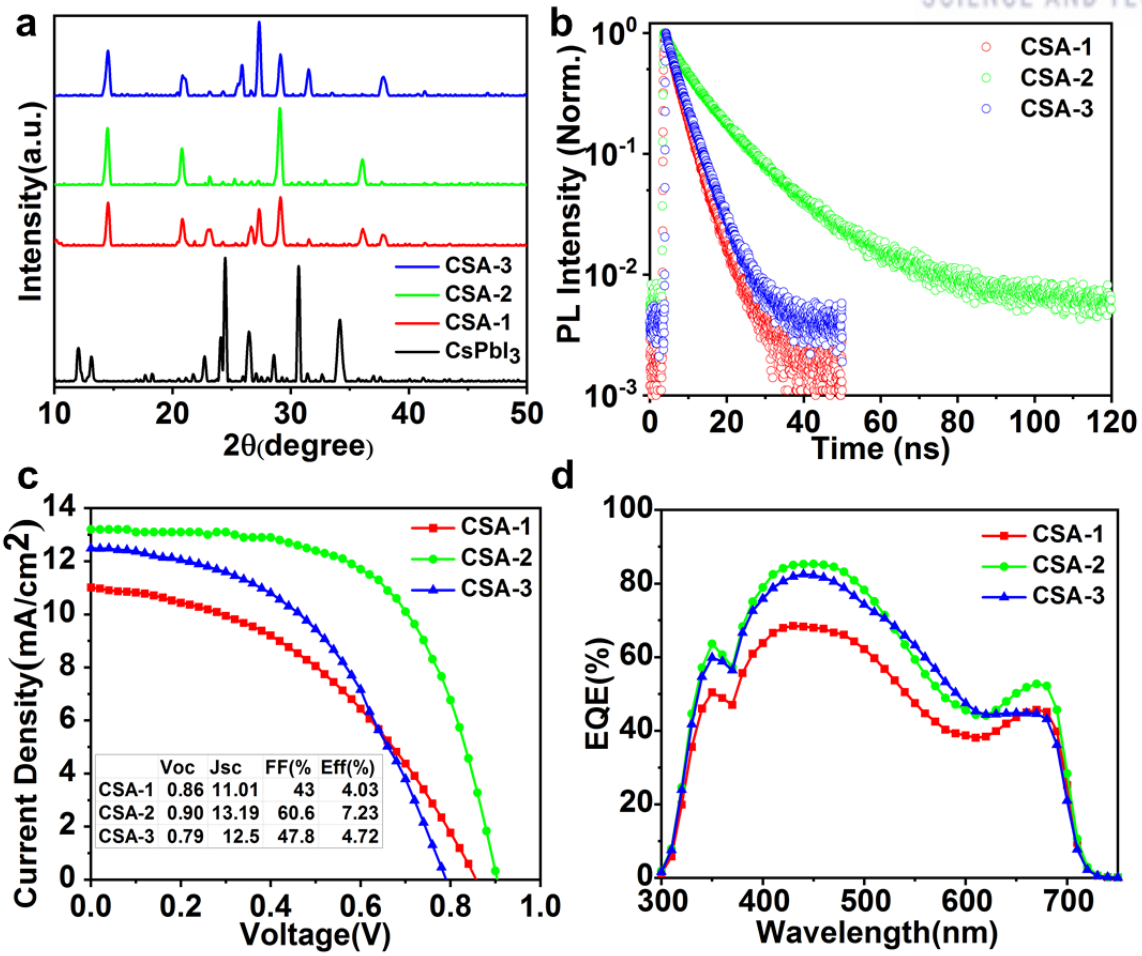

Figure 2.8 a) Comparison of X-ray diffraction (XRD) patterns for δ-$CsPbI_3$, CSA-1, CSA-2 and CSA-3. (b) Time correlated single photon counting comparison of CSA-1, CSA-2, and CSA-3. (c) PCE performance of the $CsPbI_3$ perovskite device with different doping schemes (the results of CSA (1-3) schemes were summarized in table). (d) External quantum efficiency (EQE) of CSA (1-3) schemes.

Furthermore, the thin films of $CsPbI_3$ and CSA (1-3) used for characterization were coated on glass substrates and annealed at 120°C for 10 minutes. The PMMA encapsulation was used to keep the films intact from moisture. Firstly, the yellow phase $CsPbI_3$ film processed at low temperature exhibited characteristic diffraction peaks of orthorhombic phase with a space group of *Pnma*, while CSA-1, CSA-2 and CSA-3 exhibited α-$CsPbI_3$ with main diffraction peaks of 14.27°, 20.23° and 28.98°.[29] The CSA-1 and CSA-3 films revealed the peaks of (122) plane along with the (100), (111), and (200) planes, while CSA-2 exhibited only intense (100), (111), and (200) plane peaks which signify the formation of cubic structure.[4,5,13,29,37] Finally, we observed that CSA-2 films are more air-stable and thermally stable and have better surface morphology than CSA-1 and CSA-3 films.

Time-Correlated Single Photon Counting (TCSPC) data were recorded to analyze the effect of CSA concentration on carrier lifetime. The samples were prepared for δ-$CsPbI_3$ and CSA (1-3), with glass/perovskite configuration, where the 300±30 nm thick films excited at 450 nm wavelengths were used without encapsulation (**Figure 2.8b**). However, $CsPbI_3$ processed at low temperature did not exhibit any PL intensity, so it was not possible to record carrier lifetime for comparison with CSA (1-3) samples. The fast component (τ_1) and slow component (τ_2) indicate the presence of defect states and effective recombination lifetime, respectively[7,22]. The trap state lifetimes in CSA-1 and CSA-3 samples (3.066 and 2.473 ns) were relatively similar, while the trap state lifetime in CSA-2 increased to 5.973 ns (indicating the increased excitons recombination time). Similarly, τ_2 increased from 5.905 ns for CSA-1 to 14.942 ns for CSA-2, which indicates the better surface passivation provided by the CSA-2. The increase of τ_2 to 4.809 ns for CSA-3 indicates the lower recombination lifetime. Finally, the results suggest that increasing the amount of CSA above CSA-2 gave a detrimental effect on surface passivation and carrier lifetime, and its consequences were also observed from PSC's results. The detailed lifetime results are shown in **Table S1.** The average PL decay time (τ_{avg}) exhibited the improved charge dissociation and transport in CSA-2 compared with CSA-1 and CSA-3, so these results suggest the CSA-2 to be optimal for device fabrication.

Table S1. Lifetime measurement results of the perovskite thin films.

Condition	τ_1 (ns)	f_1 (%)	τ_2 (ns)	f_2 (%)	τ_{avg} (ns)	χ^2
CSA-1	3.066	79.46	5.905	20.54	**3.649**	1.02
CSA-2	5.973	56.28	14.942	43.72	**9.894**	1.09
CSA-3	2.473	27.01	4.809	72.99	**4.178**	1.01

In order to obtain chemical information and study the distribution of all the components in inorganic perovskite, Time-of-Flight secondary ion mass spectrometry (TOF-SIMS) was used in three dimensions (a combination of high-resolution imaging with depth profiling). The information of Cs, Pb, and Ba distribution throughout the perovskite layer deposited on a glass substrate by one-step solution process was gathered (**Figure 2.9**).

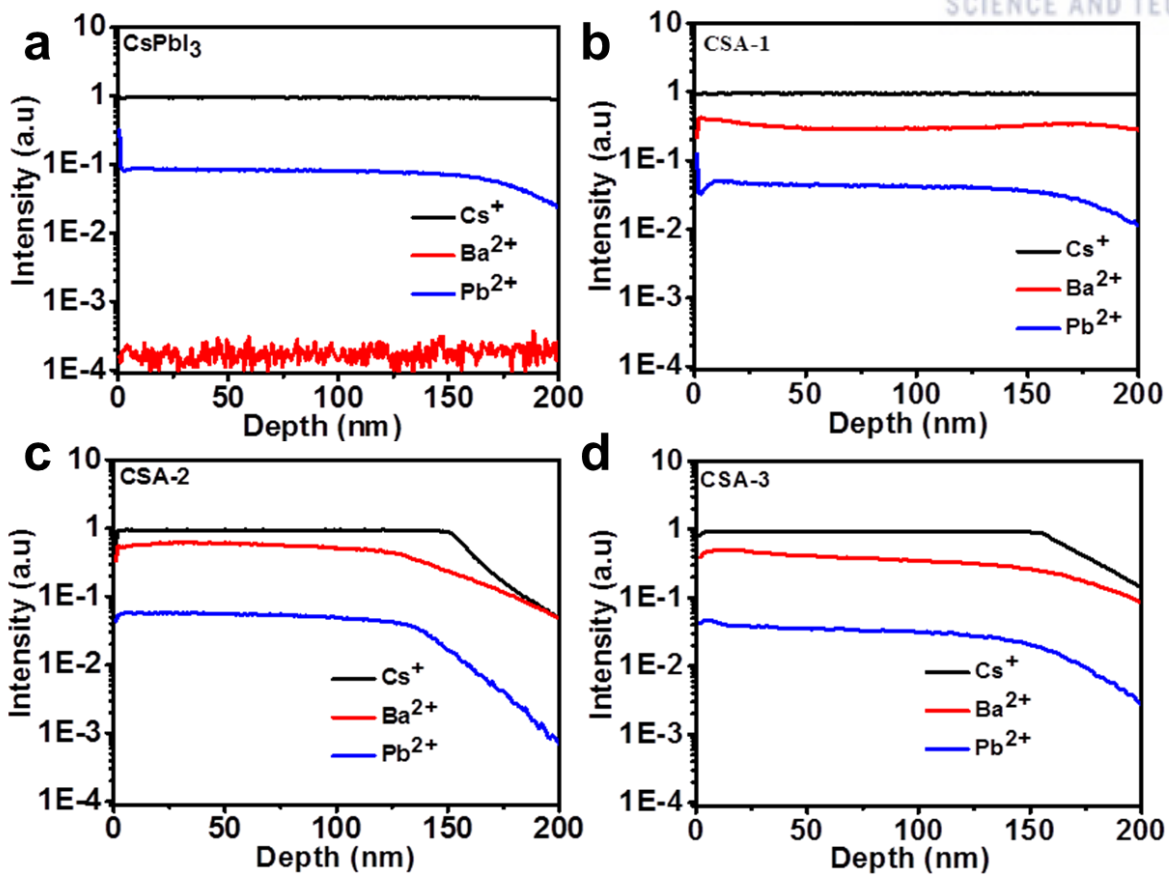

Figure 2.9. a) Depth profile of a $CsPbI_3$ perovskite films processed at room temperature, the Cs, Pb, and Ba curves represents the chemical composition and their uniformity inside the film. b) The variation in intensity of Cs, Pb, and Ba depth profiles, which indicates the uniformity of CSA-1 components in scheme. c) Depth profiling of CSA-2. d) Depth profiling of CSA-2. Film thickness: (~200±50 nm).

2.4.6. TOF-SIMS Analysis

The film thickness of the samples was ~200±50 nm. We used standard profiling conditions with a 0.5 keV oxygen sputter beam (95-100 nA sputter current) for the perovskite layer. The distribution of Cs^+ and Pb^{2+} cations was uniform throughout the film, while inhomogeneity in Ba^{2+} distribution was observed from the depth profiling measurements in CSA (1-3) samples (**Figure 2.10**), mainly because of the minor ratio of Ba^{2+} to Pb^{2+} at the B-site.

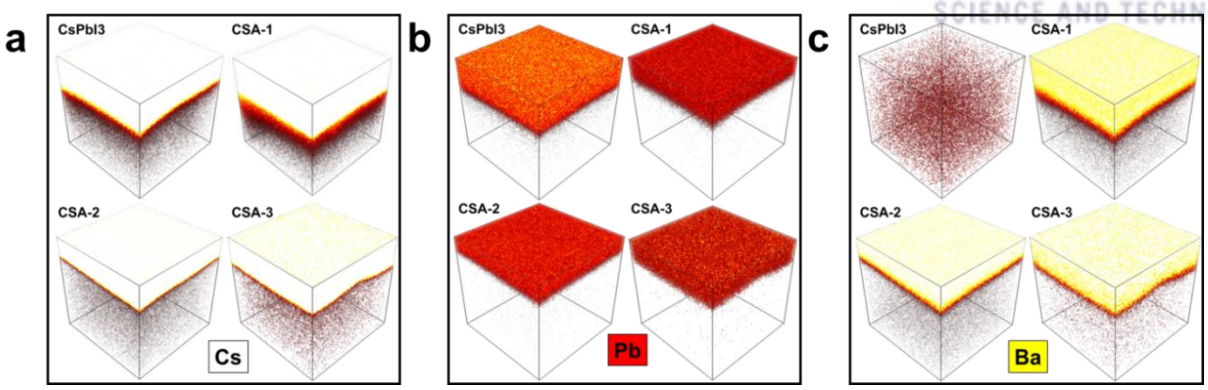

Figure 2.10. TOF-SIMS 3D tomography results for inorganic perovskite processed at low temperature. 3D image of four films with $CsPbI_3$, CSA-1, CSA-2, and CSA-3 schemes showing a) Cs (white color) element depth profiling with film thickness (~200±50 nm), b) Pb in red color, and c) Ba in color yellow. 3D reconstruction dimension is 50 × 50 × 0.5 μm^3.

The inorganic perovskite films were used as the absorber material to fabricate planar PSCs with configuration of ITO/SnO_2/perovskite/P3HT/Au. The deposition of inorganic hole transport layer (HTL) material makes the fabrication process complicated for the commercial use; so we used all solution based materials and the devices were processed below 150°C. We fabricated the device with 2, 5, and 10% Ba doping, while optimizing the amount of doping concentration with CSA additive. The PCE values of the devices with 2, 5 and 10% Ba-doping concentration are shown in **Figure 2.8c, 2.11.**

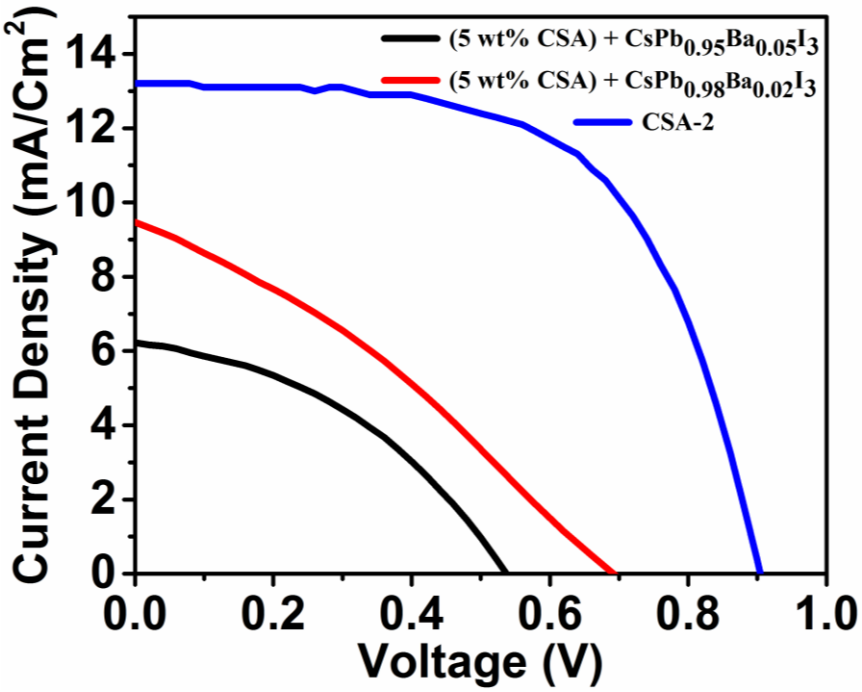

Figure 2.11. PCE performance of the $CsPbI_3$ perovskite device with different doping concentration of Ba having 5 wt% CSA as additive.

The devices with CSA-2 exhibited significant PCE of 7.23%. The devices were stable inside glove box and retained ~98 % of its initial PCE values even after 500 h of continuous white LED illumination, which indicated a photo-stable and moisture-resistant PSCs (**Figure 2.11**). The stability of devices was observed after exposing them to open air with 50-60% relative humidity at room temperature for 1 h, and the devices retained ~99% of their initial value.

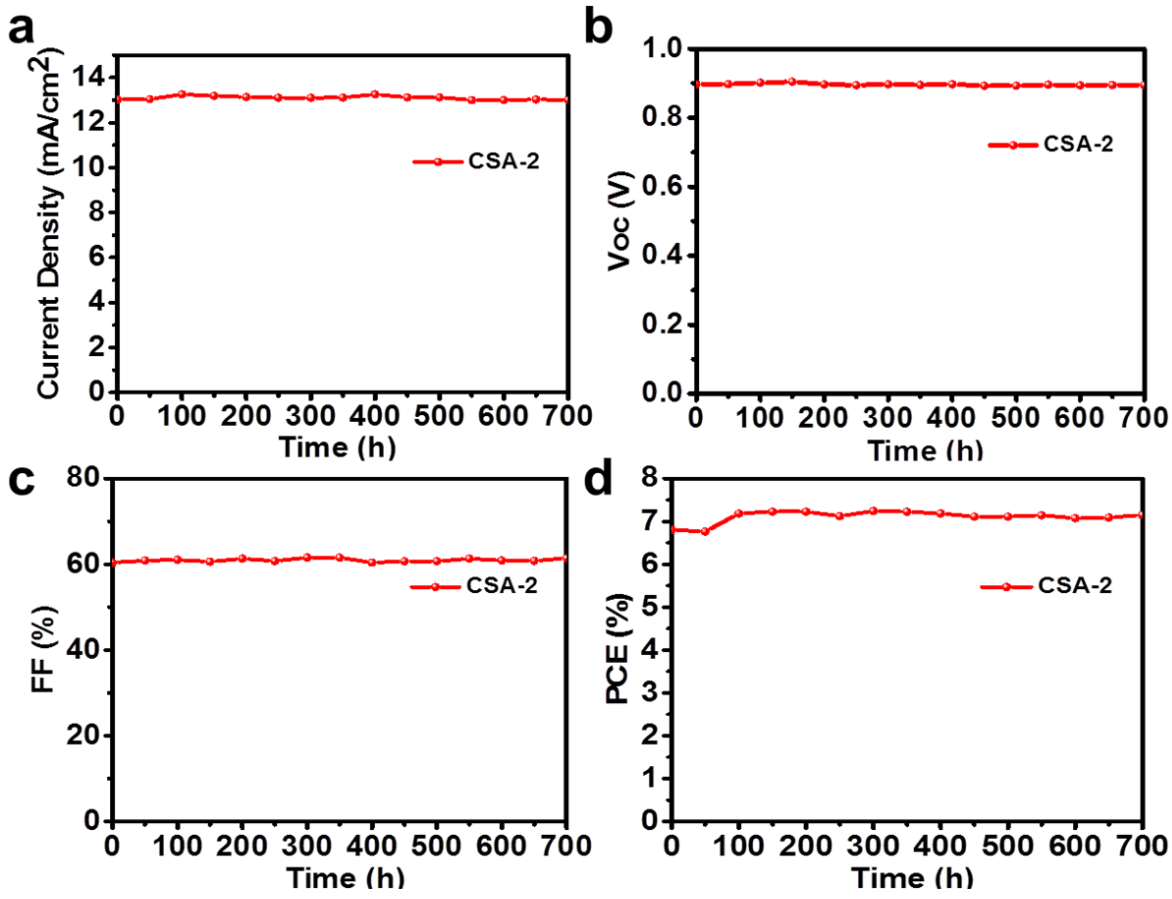

Figure 2.12. Photostability and moisture stability investigation of the best performing perovskite solar cells device (CSA-2) without any encapsulation under nitrogen atmosphere. a) Short Circuit Current Density (Jsc) recorded at AM 1.5 G condition. b) Open Circuit Voltage (Voc). c) Fill factor (FF). d) Power conversion efficiency. Slight increase, in particular, in PCE was observed after aging for 100 h.The X-ray diffraction patterns were also recorded after one year for the thin films stored inside glove box without encapsulation as shown in **Figure 2.12.**

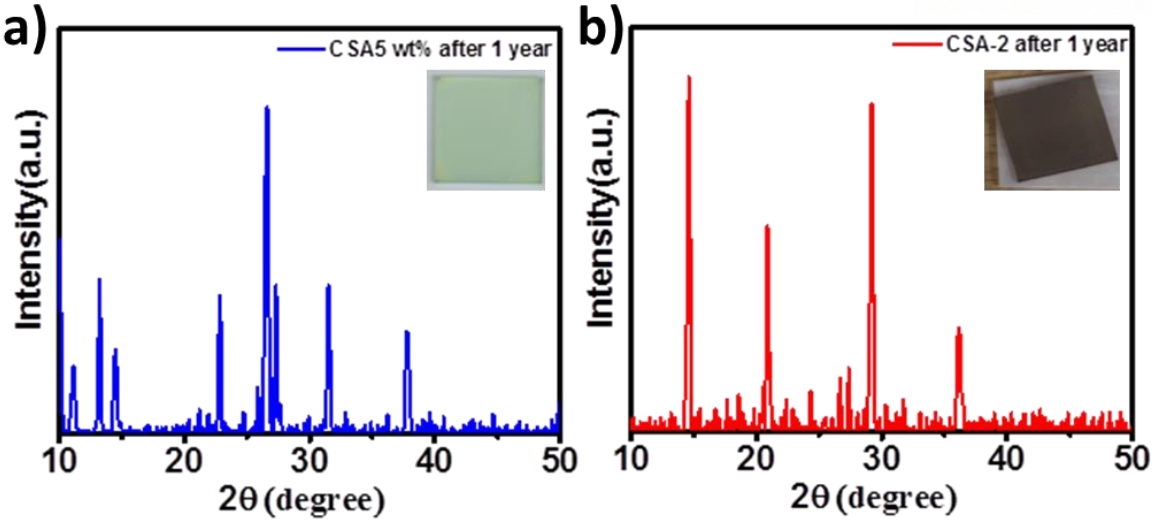

Figure 2.13. X-ray diffraction (XRD) patterns. a) CSA 5wt % additive with $CsPbI_3$ and b) CSA-2 samples, after 1 year of storage under ambient conditions (Inset: photographs of the thin films).

To validate the characterization of devices, the incident photo to current efficiency (IPCE) measurement was conducted using the best cells, and the results were in good agreement with the current density recorded from the current-voltage measurement (**Figure 2.8d**). The performance of the best cells with different concentration is summarized in **Figure 2.9c**, the CSA-2 PSCs exhibited the highest PCE values among all the schemes which make a good correlation with the XRD, TCSPC and FE-SEM images.

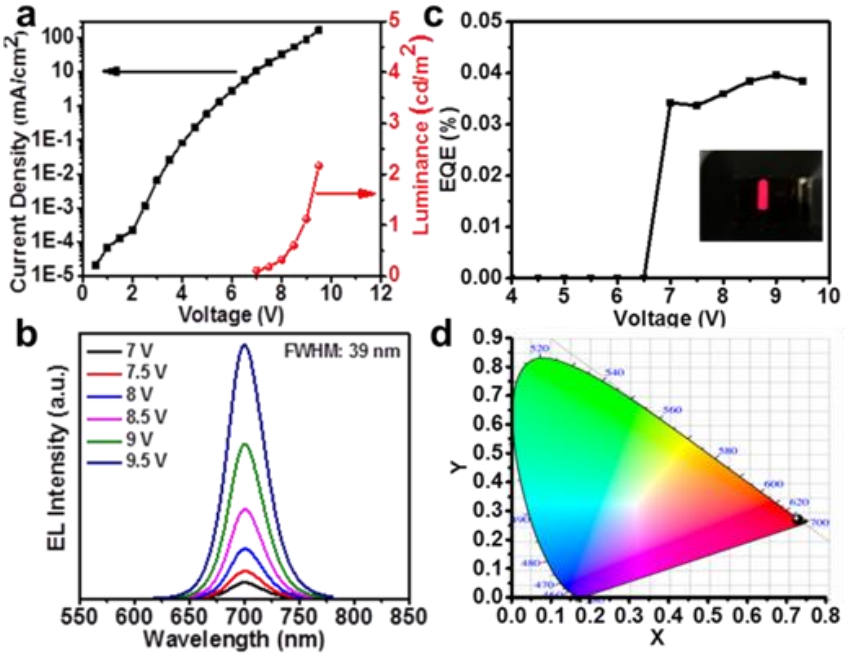

Figure 2.14 Current density-voltage-luminance (J-V-L) characteristic of $CsPbI_3$ with optimized CSA-2 scheme. b) External quantum efficiency characteristics of red-light-emitting PLED (inset:

photograph showing the red light-emission from the device). c) Electroluminescence spectrum of CSA-2 LED device. d) CIE coordinates of the fabricated device.

Furthermore, the optimized condition of perovskite material after successful fabrication of solar cells was used to check the possibilities with perovskite LEDs (PLEDs). The CSA-2 perovskite thin films have homogenous crystal grain size of ~100 nm, which motivated us to check the possibilities for PLEDs with bulk material properties. We successfully fabricated PLED devices with a conventional architecture of ITO/PEDOT:PSS/perovskite/TPBi/LiF/Al to evaluate its performance as light emitter. A red-light-emission was observed at 700 nm with an FWHM of 39 nm exhibiting a narrow emission region (**Figure 2.14b, c**). We also achieved a turn-on voltage of 7 V (@ 0.1 cd m^{-2}) (**Figure 14b**), and PLEDs showed maximum brightness and EQE of 2.17 cd m^{-2} and 0.04% (**Figure 14a**). The International Commission on Illumination (CIE) coordinates of the fabricated device are shown in **Figure 14d**. Although we did not consider the $CsPbI_3$ energy band alignment with the transporting materials, we observed a red-light-emission. Further, improvements can be made by selecting the proper transporting materials. From this experiment we observed that Ba-doped $CsPbI_3$ is a strong candidate for future tandem solar cells and optoelectronic devices.

2.5. Conclusion

In summary, for the first time, we successfully stabilized the α-$CsPbI_3$ by incorporating barium with the optimal amount (~10 %) that well matches with DFT calculations and it exhibited more thermal and photo-stable films without compromising the optical properties. Initially, we observed that Ba-doped thin films without CSA incorporation had poor air stability. Later, we incorporated CSA and found that it improved the air stability. We performed HPXRD characterization in the open air and observed that the thin films with Ba degraded immediately upon air exposure, while CSA-2 samples were stable in air. We noticed that the thin films were stable in ambient air condition for one year. The solution-processed typical planar PSCs and PLEDs were fabricated without encapsulation to validate the applicability. The active layer deposited by one-step solution processing exhibited better thermal, photo, phase, and air stability and the PSCs exhibited impressive power conversion efficiency. The fabricated devices were exposed to open air with 50-60% relative humidity for ~1 h, and the devices retained 99 % of its initial values. Interestingly, the fabricated PSCs retained high stability and attained ~98% of its initial value even after 700 h, which strongly supports their non-volatile behavior of $CsPbI_3$ perovskite and its future potential applications. Also, the PLEDs were fabricated using the ITO/PEDOT:PSS/ perovskite/TPBi/LiF/Al structure, which exhibited a red-light emission at 700 nm. The combination of surface passivation and metal substitution together offers better air and thermal stability, which opens a new direction for highly stable perovskite optoelectronics devices.

2.6. References

1 N.G. Park, M. Grätzel, T. Miyasaka, K. Zhu and K. Emery, *Nat. Energy*, 2016, **1**, 16152.

2 N. J. Jeon, H. Na, E. H. Jung, T. Y. Yang, Y. G. Lee, G. Kim, H. W. Shin, S. Il Seok, J. Lee and J. Seo, *Nat. Energy*, 2018, **3**, 682–689.

3 Woon Seok Yang, Byung-Wook Park, Eui Hyuk Jung, Nam Joong Jeon, Young Chan Kim, Dong Uk Lee, Seong Sik Shin, Jangwon Seo, Eun Kyu Kim, Jun Hong Noh and Sang Il Seok, *Science*, 2017, **356**, 1376–1379.

4 Y. Wang, T. Zhang, M. Kan and Y. Zhao, *J. Am. Chem. Soc.*, 2018, **140**, 12345–12348.

5 Y. Hu, F. Bai, X. Liu, Q. Ji, X. Miao, T. Qiu and S. Zhang, *ACS Energy Lett.*, 2017, **2**, 2219–2227.

6 P. Wang, X. Zhang, Y. Zhou, Q. Jiang, Q. Ye, Z. Chu, X. Li, X. Yang, Z. Yin and J. You, *Nat. Commun.*, 2018, **9**, 1–7.

7 X. Wen, Y. Feng, S. Huang, F. Huang, Y. B. Cheng, M. Green and A. Ho-Baillie, *J. Mater. Chem. C*, 2015, **4**, 793–800.

8 J. Lin, M. Lai, L. Dou, C. S. Kley, H. Chen, F. Peng, J. Sun, D. Lu, S. A. Hawks, C. Xie, F. Cui, A. P. Alivisatos, D. T. Limmer and P. Yang, *Nat. Mater.*, 2018, **17**, 261–267.

9 H. Kang, S. Jung, H. Back, K. Lee, J.-H. J. J.-H. J. J.-H. Lee, J.-H. J. J.-H. J. J.-H. Lee, S. Hong, S. Kim, G. Kim, S. Kee, K. Yu, B. Park, J.-H. J. J.-H. J. J.-H. Lee, H. Kang, G. Kim, S. Kee, J.-H. J. J.-H. J. J.-H. Lee, S. Jung, B. Park, S. Kim, H. Back, K. Yu and K. Lee, *Sci. Adv.*, 2018, **4**, eaat3604.

10 Abhishek Swarnkar, A. R. Marshall, E. M. Sanehira, D. T. M. Boris D. Chernomordik and J. M. L. Jeffrey A. Christians, Tamoghna Chakrabarti, *Science*, 2016, **354**, 92–96.

11 J. Liang, P. Zhao, C. Wang, Y. Wang, Y. Hu, G. Zhu, L. Ma, J. Liu and Z. Jin, *J. Am. Chem. Soc.*, 2017, **139**, 14009–14012.

12 J. Gong, P. Guo, S. E. Benjamin, P. G. Van Patten, R. D. Schaller and T. Xu, *J. Energy Chem.*, 2018, **27**, 1017–1039.

13 G. E. Eperon, G. M. Paternò, R. J. Sutton, A. Zampetti, A. A. Haghighirad, F. Cacialli and H. J. Snaith, *J. Mater. Chem. A*, 2015, **3**, 19688–19695.

14 A. Marronnier, G. Roma, S. Boyer-Richard, L. Pedesseau, J. M. Jancu, Y. Bonnassieux, C. Katan, C. C. Stoumpos, M. G. Kanatzidis and J. Even, *ACS Nano*, 2018, **12**, 3477–3486.

15 Y. J. Choi, L. Debbichi, D. K. Lee, N. G. Park, H. Kim and D. Kim, *J. Phys. Chem. Lett.*, 2019, **10**, 2135–2142.

16 Q. Wang, X. Zheng, Y. Deng, J. Zhao, Z. Chen and J. Huang, *Joule*, 2017, **1**, 371–382.

17 Y. Fu, M. T. Rea, J. Chen, D. J. Morrow, M. P. Hautzinger, Y. Zhao, D. Pan, L. H. Manger, J. C. Wright, R. H. Goldsmith and S. Jin, *Chem. Mater.*, 2017, **29**, 8385–8394.

18 G. Grancini, C. Roldán-Carmona, I. Zimmermann, E. Mosconi, X. Lee, D. Martineau, S. Narbey, F. Oswald, F. De Angelis, M. Graetzel and M. K. Nazeeruddin, *Nat. Commun.*, 2017, **8**, 15684.

19 C. Liu, W. Li, H. Li, H. Wang, C. Zhang, Y. Yang, X. Gao, Q. Xue, H. L. Yip, J. Fan, R. E. I. Schropp and Y. Mai, *Adv. Energy Mater.*, 2019, **9**, 1–9.

20 C. Liu, W. Li, C. Zhang, Y. Ma, J. Fan and Y. Mai, *J. Am. Chem. Soc.*, 2018, **140**, 3825–3828.

21 R. A. Scheidt, C. Atwell and P. V. Kamat, *ACS Mater. Lett.*, 2019, 8–13.

22 C. F. J. Lau, M. Zhang, X. Deng, J. Zheng, J. Bing, Q. Ma, J. Kim, L. Hu, M. A. Green, S. Huang and A. Ho-Baillie, *ACS Energy Lett.*, 2017, **2**, 2319–2325.

23 W. Xiang, Z. Wang, D. J. Kubicki, W. Tress, J. Luo, D. Prochowicz, S. Akin, L. Emsley, J. Zhou, G. Dietler, M. Grätzel and A. Hagfeldt, *Joule*, 2019, **3**, 205–214.

24 C. F. J. Lau, X. Deng, J. Zheng, J. Kim, Z. Zhang, M. Zhang, J. Bing, B. Wilkinson, L. Hu, R. Patterson, S. Huang and A. Ho-Baillie, *J. Mater. Chem. A*, 2018, **6**, 5580–5586.

25 Y. Hu, F. Bai, X. Liu, Q. Ji, X. Miao, T. Qiu and S. Zhang, *ACS Energy Lett.*, 2017, **2**, 2219–2227.

26 B. Li, Y. Zhang, L. Fu, T. Yu, S. Zhou, L. Zhang and L. Yin, *Nat. Commun.*, 2018, **9**, 1–8.

27 P. Luo, W. Xia, S. Zhou, L. Sun, J. Cheng, C. Xu and Y. Lu, *J. Phys. Chem. Lett.*, 2016, **7**, 3603–3608.

28 Z. Chu, M. Yang, P. Schulz, D. Wu, X. Ma, E. Seifert, L. Sun, X. Li, K. Zhu and K. Lai, *Nat. Commun.*, 2017, **8**, 1–8.

29 B. Jeong, H. Han, Y. J. Choi, S. H. Cho, E. H. Kim, S. W. Lee, J. S. Kim, C. Park, D. Kim and C. Park, *Adv. Funct. Mater.*, 2018, **28**, 1–8.

30 J. P. Perdew, K. Burke and M. Ernzerhof, 1996, 3865–3868.

31 A. Tkatchenko, R. A. Distasio, R. Car and M. Scheffler, *Phys. Rev. Lett.*, 2012, **108**, 1–5.

32 Y. G. Kim, T. Y. Kim, J. H. Oh, K. S. Choi, Y. J. Kim and S. Y. Kim, *Phys. Chem. Chem. Phys.*, 2017, **19**, 6257–6263.

33 T. Yoon, G.-H. Kim, C. W. Myung, S. Kajal, J. Jeong, J. W. Kim, J. Y. Kim and K. S. Kim, *ACS Appl. Energy Mater.*, 2018, **1**, 5865–5871.

34 J. Liang, C. Wang, P. Zhao, Z. Lu, Y. Ma, Z. Xu, Y. Wang, H. Zhu, Y. Hu, G. Zhu, L. Ma, T. Chen, Z. Tie, J. Liu and Z. Jin, *Nanoscale*, 2017, **9**, 11841–11845.

35 M. Deepa, M. Salado, L. Calio, S. Kazim, S. M. Shivaprasad and S. Ahmad, *Phys. Chem. Chem. Phys.*, 2017, **19**, 4069–4077.

36 C. Wang, A. S. R. Chesman and J. J. Jasieniak, *Chem. Commun.*, 2017, **53**, 232–235.

37 T. Zhang, M. I. Dar, G. Li, F. Xu, N. Guo, M. Grätzel and Y. Zhao, *Sci. Adv.*, 2017, **3**, e1700841.

38 R. J. Sutton, M. R. Filip, A. A. Haghighirad, N. Sakai, B. Wenger, F. Giustino and H. J. Snaith, *ACS Energy Lett.*, 2018, **3**, 1787–1794.

Chapter 3

Unfolding the Influence of Metal Doping on Properties of $CsPbI_3$ Perovskite

3.1. Abstract

Low-temperature α-phase stabilization using HI or zwitterions in cesium lead iodide ($CsPbI_3$) endures the metastable phase properties but is thermally unstable. Doping with a small amount of heterovalent metals (i.e. Bi^{3+}, Sb^{3+}) in $CsPbI_3$ has been assumed to stabilize the α-phase, while here we challenge this assumption. We demonstrate that heterovalent metal ion doping stabilizes β-$CsPbI_3$ at low temperatures without replacing the Pb^{2+} cations, while divalent cations (i.e., Ba^{2+}, Sr^{2+}, and Sn^{2+}) doping stabilizes the α-$CsPbI_3$ by replacing the Pb^{2+} cations. This finding is demonstrated by both theoretical and experimental results. We also find that the divalent cations stabilize α-$CsPbI_3$ films, making thermally stable at high temperatures, whereas heterovalent metal-doping stabilizes β-$CsPbI_3$ films, making metastable. The doping influence on crystal grains and the chemical composition of thin films is discussed. In particular, the charge dissociation kinetics for the Sr doped thin film are much enhanced than α-$CsPbI_3$ and Ba doped thin films, and the initial results of the fabricated perovskite red-light-emmiting diode suggests that the Sr-doped thin films would be more suitable for the device fabrication. These findings will guide a way for further development in thermally and air-stable optoelectronic devices.

3.2. Introduction

Inorganic lead halide perovskite gained a considerable attention due to its non-volatile nature of inorganic cations. It offers higher thermal and photo-stability compared to organic-inorganic perovskites. Usually, $CsPbI_3$ has (photo-inactive) δ-phase at room temperature. Thus, tremendous research efforts have been made to stabilize the (photo-active) α-phase at room temperature. As a consequence, inorganic perovskite solar cells achieved efficiency from ~2.4% to 18%, within a short period.[1–3] In particular, excess HI stabilizes the black phase at room temperature, but a metastable phase persists in perovskite, which transforms black to yellow phase upon annealing at high temperatures.[4–7] Various results reveal the existence of polymorph nature in $CsPbI_3$ which remains less stable than the yellow non-perovskite polymorph.[8,9] Also, doping of metal cations besides excessive HI was reported to stabilize the α-phase of $CsPbI_3$[10], and these materials based perovskite solar cells (PSCs) achieved attractive efficiencies.[5,11] Earlier, Eu^{3+} doping in $CsPbI_2Br$ suppressed the non-radiative charge recombination, and a high open-circuit voltage (V_{oc}) of 1.27 V was achieved, with a high power conversion efficiency (PCE) of 13.71%.[12] Also Hu et al. reported that the incorporation of 4 mol % Bi^{3+} stabilizes the α-phase of $CsPbI_3$, achieving a high PCE of 13.21%.[13] Lau et al. reported that 5mol % Ca^{2+} incorporation in $CsPbI_3$ stabilized the α-phase, achieving 13.3%,

but it increased the band gap.[14] Liang et al. reported $CsPb_{0.9}Sn_{0.1}IBr_2$ based PSC's with a V_{oc} of 1.26 V and a PCE of 11.33%.[15] Lau et al. reported that low-temperature-processed $CsPb_{0.98}Sr_{0.02}I_2Br$ achieved a stabilized PCE of 10.8% and Sr provided a passivation effect in the perovskite film.[16] However, metal-doped $CsPbI_3$ lacks behind in efficiency compared to ligands incorporated γ-$CsPbI_3$.[1,2,6,7,17,18] Some reports based on Bi^{3+}, Sb^{3+}, and Eu^{3+} assumed stabilization of the α-phase of $CsPbI_3$,[19][10][13] but their structural data revealed the presence of the distorted β-phase. To investigate if the α-phase stabilization assumption is valid, we performed electronic band gap calculations for Ba^{2+}, Sr^{2+}, Sn^{2+}, Sb^{3+}, and Bi^{3+} doped $CsPbI_3$, and studied the optimized defect formation energy for perovskite formation. For Sb^{3+} (or Bi^{3+}) doping, three Pb^{2+} ions are doped with two Sb^{3+} (or Bi^{3+}) ions with one Pb^{2+} vacant site to maintain the charge balance. In this regard, we deposited thin films based on the theoretically optimized concentration of metal doping. The obtained thin films, in particular, Sr^{2+} doped films were highly thermally stable with better photo-stability, compared to the camphor sulfonic acid (CSA) stabilized $CsPbI_3$. Here we discuss the details of our ab initio thermodynamic modeling and thin-film characteristics to verify the structural stability, phase formation energy, doping concentration, and band gap changes.

3.3. Experimental Section

3.3.1. Materials

Barium iodide (BaI_2, 99.9%), antimony iodide (SbI_3, 99.999%), tin iodide (SnI_2, 99.9%), (1S)-(+)-10-camphor sulfonic acid (CSA, 99%), cesium iodide (CsI,99.9%), lead iodide (PbI_2,99.9%), bismuth iodide (BiI_3, 99.998%), strontium iodide (99.9%), N,N-dimethylformamide (DMF, anhydrous, 99.8%), and all other chemicals including dimethyl sulfoxide (DMSO, anhydrous, 99.8%) were purchased from Sigma-Aldrich. All salts and solvents were used as received without any further purification.

3.3.2. Precursor Solution Preparation

All metal doped precursor solutions were prepared by dissolving CsI and $Pb_{1-x}M_xI_3$ (where M is metal dopant) in 1:1 mmol stochiometric solution, where the amount of x is 0.04 for SbI_3 and BiI_3, while the amount of x is 0.10 for BaI_2, SrI_2, and SnI_2. The $CsPbI_3$ precursor solution was prepared by dissolving CsI and PbI_2 (1:1 mmol) and additional CSA (10 wt% of precursor salt) was added with a mixture of DMSO and DMF (6:4 in volume) as solvent.

3.3.3. Thin Film Deposition

Firstly, glass substrate was ultrasonically cleaned by detergent, deionized water, acetone and isopropyl alcohol for 10 min each and then treated by a UV/O_3 cleaner for 30 minutes. The perovskite layer was deposited by one step spin-coating method using the 1 mM $CsPb_{1-x}M_xI_3$ precursor solution

at the speed of 3,000 rpm for 30 s followed by annealing at 60°C for 1 minute and then at 100°C for 10 minutes.

3.3.4. Characterization and measurements

The thin films were characterized by UV-Vis-NIR (Carry 5000, Agilent) for measuring the absorption properties, while the PL was measured with fluorometer (Carry Eclipse, Agilent), excited at 400 nm. Also, the surface morphology of perovskite thin films with/without metal doping was analyzed by field emission SEM (Nova NanoSEM, FEI). Further, the chemical composition of the samples were investigated by XPS (K-alpha, ThermoFisher). Finally, the crystallographic information was determined with scanning angle 2θ ranging from 10° and 50° by using a high-power XRD (MAX 2500V, Rigaku) with Cu Kα radiation (λ = 1.54059 Å). Time-resolved and steady-state PL spectra were measured by using FluoTime 300. The samples were photoexcited with a 510 nm continuous wave and pulsed diode laser head (LDH-D-C-510). The PL decay curves were fitted to a biexponential decay model using software, FluoFit.

3.3.5. Density functional theory calculations

DFT calculations were performed using the Vienna Ab initio Simulation Package (VASP) [31] suite with the PBE exchange-correlation functional.[32] Structural geometry optimization was performed with energy convergence and force convergence of 10^{-6} eV and 0.02 eV/Å, respectively. We employed *G*-centered (2 × 2 × 2) *k*-point mesh for sampling the Brillouin zone (BZ) and 500 eV energy cutoff for the PAW plane-wave basis sets. The (3 × 3 × 3) supercell of cubic $CsPbI_3$ wa used for Ba^{2+}, Sr^{2+}, Sn^{2+}, Sb^{3+}, and Bi^{3+}doping and the (2 × 4 × 1) supercell of orthorhombic $CsPbI_3$ was used for Ba^{2+}, Sr^{2+}, Sn^{2+}, Sb^{3+}, and Bi^{3+}doping. The E_f is defined as the following equation (Z: Ba, Sr, Sn, Sb, Bi, N: the number of dopant atoms).[33]

$$E_f = E(CsPb_{1-x}Z_xI_3) - E(CsPbI_3) + N \times (E(Pb) - E(Z)) \quad (1)$$

$E(CsPb_{1-x}Z_xI_3)$ is the total energy of the doped system, $E(CsPbI_3)$ is the total energy of $CsPbI_3$supercell of equal size, N is the number of dopant atoms, and E(Pb) and E(Z) are the bulk energy per atom Pb and dopant element Z.

3.4. Results and Discussion

It is a well-known that replacing iodide (I^-) by bromide (Br^-) by more than one third stabilizes the α-phase of $CsPbI_3$, but this results in increased bandgap.[20,21] There are limited studies on metal-doped α-phase stabilization of $CsPbI_3$.[22] Here, we study the doping effects of divalent metals (having similar oxidation state i.e., Sr^{2+}, Ba^{2+}), heterovalent metals (having dissimilar oxidation state i.e., Sb^{3+}, Bi^{3+}) and a post-transition metal with SnI_2 (having more than one oxidation state i.e., Sn^{2+}, Sn^{4+}),

using only their iodide salts to stabilize α-phase of $CsPbI_3$. The effects of doping on thermal and air stability were observed after annealing and air exposure, respectively.

3.4.1. DFT analysis

To determine the optimum concentration of doping, DFT calculations were performed, and the obtained defect formation energy is summarized in **Table S1**. The detailed method of the formulation is explained in the experimental section. The minimum formation energies for cubic structure were obtained at concentrations 11.10%, 11.10%, 11.10%, 3.70%, and 3.70% for Ba^{2+}, Sr^{2+}, Sn^{2+}, Sb^{3+}, and Bi^{3+}, respectively, while the minimum formation energies for orthorhombic structure were obtained at concentrations 9.4%, 9.4%, 9.4%, 3.1%, and 3.1%. For thin film deposition, we used our earlier optimized 10 wt% doping concentration for BaI_2 and a similar amount was used for SrI_2, and SnI_2, while 4wt % doping was used for both SbI_3 and BiI_3 for the ease of weighing. According to DFT calculations on the doping by Sr^{2+}, Ba^{2+}, Sn^{2+}, Sb^{3+}, and Bi^{3+}, we note that Sr, Sn, and Ba dopings stabilize the α-phase, while Sb and Bi dopings stabilize the distorted β-phase. This trend could also be verified by theoretical defect formation energy (E_f) calculations (**Table S1**). The positive value of E_f indicates the amount of energy required to substitute a single Pb atom by a dopant. For Ba^{2+}, Sr^{2+}, and Sn^{2+} doped systems, the E_f of cubic structures ($E_{f.cubic}$) are 2.32 eV, 1.04 eV, and 0.31 eV more stable than those of orthorhombic structures ($E_{f.ortho}$), respectively. In contrast, $E_{f.cubic}$ is only 0.06 eV more stable than $E_{f\ ortho}$ for Sb^{3+} doped system, and 0.03 eV less stable than that for the Bi^{3+} doped system. Even though the theoretical result for Sb^{3+} doped system looks opposite to the experimental result, it is consistent with the experiment in that the magnitude is near zero. In particular, the degree of its stability is much less than Ba^{2+}, Sr^{2+}, and Sn^{2+} doped systems. Therefore, the results qualitatively elucidate that Ba^{2+}, Sr^{2+}, and Sn^{2+} stabilize the α-phase, while Sb^{3+} and Bi^{3+} stabilize the distorted β-phase of the perovskite.

Table 1. DFT-predicted defect formation energy (eV), of a-$CsPb_{(1-x)}Z_xI_3$ ($E_{f.cubic}$) and b-$CsPb_{(1-x)}Z_xI_3$ ($E_{f.ortho}$) for the doped perovskite (Z = Ba, Sr, Sn, Sb, and Bi). The doping concentration x is given in parentheses.

$E_{f.cubic}$	Ba (11.1%)	Sr (11.1%)	Sn (11.1%)	Sb (3.7%)	Bi (3.7%)
	-10.53	-9.03	0.64	1.40	1.37
$E_{f.ortho}$	Ba (9.4%)	Sr (9.4%)	Sn (9.4%)	Sb (3.1%)	Bi (3.1%)
	-8.21	-7.99	0.95	1.46	1.34
$E_{f.cubic} - E_{f.ortho}$	-2.32	-1.04	-0.31	-0.06	0.03

Table 2. DFT-predicted band gap (eV), of a-$CsPb_{(1-x)}Z_xI_3$ ($E_{f.cubic}$) and b-$CsPb_{(1-x)}Z_xI_3$ ($E_{f.ortho}$) structure of doped perovskite (Z = Ba, Sr, Sn, Sb, and Bi). The doping concentration x is given in parenthesis.

Band gap (eV)	
Ba (11.1%)	1.92
Sr (11.1%)	1.59
Sn (11.1%)	1.20
Sb (3.7%)	1.13
Bi (3.7%)	1.18

3.4.2. Optical properties

The $CsPbI_3$ thin films were obtained by dissolving the precursor salt in a mixed solvent of dimethyl sulfoxide (DMSO) and N, N-dimethylformamide (DMF) in the ratio of 6:4, respectively. The detailed deposition method is explained in the experimental section. The mechanism of phase transformation was observed for the thin films during the annealing process, and we summarized the results with schematic illustration, as shown in **Figure 3.1a**. The samples

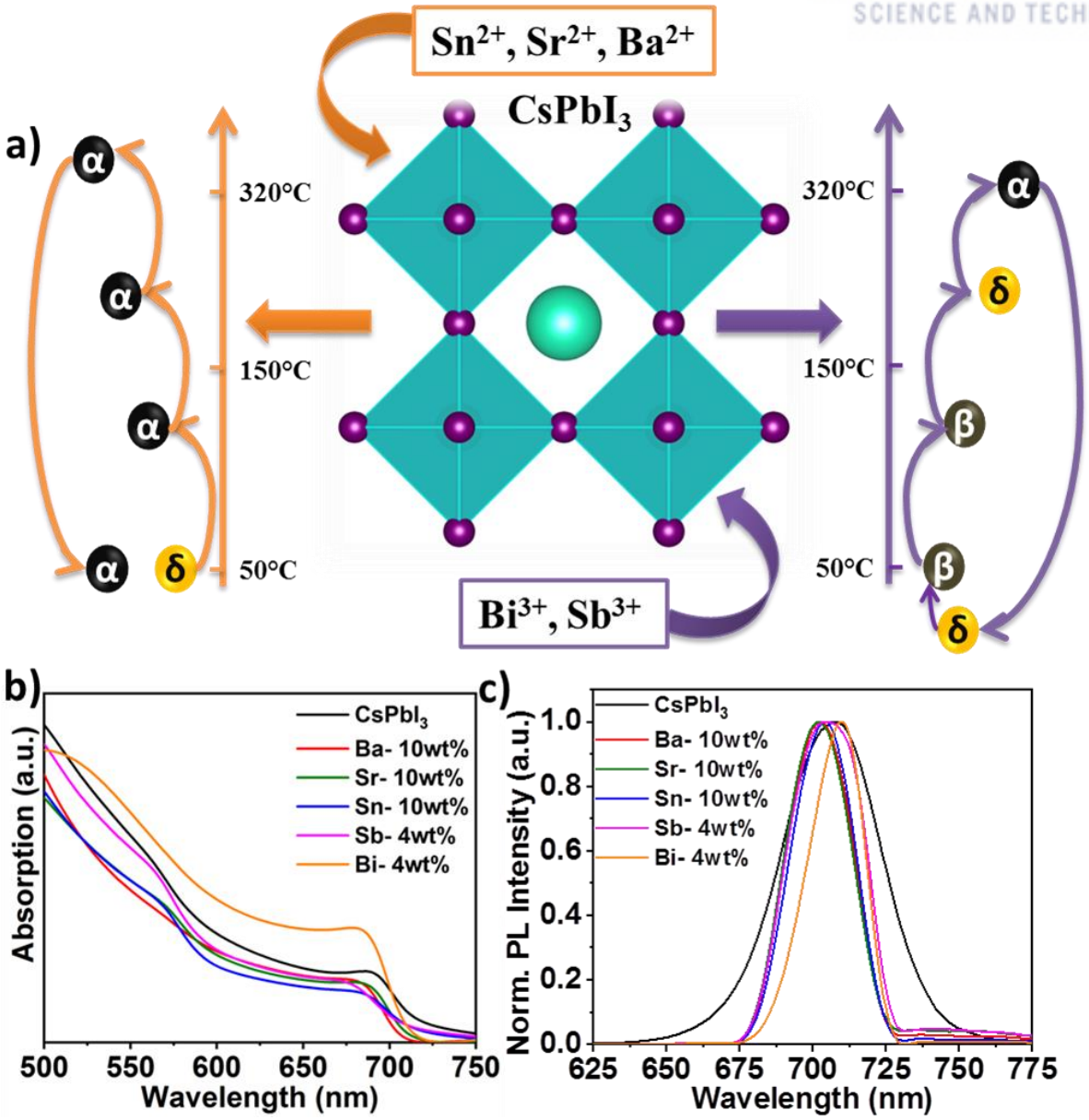

Figure 3.1. Schematic illustration of metal doping and optical properties of the metal doped thin films. (a) Illustration of the thin film structural properties with temperature: divalent dopants (left side) and heterovalent dopants (right side). (b) Absorption properties of metal doped $CsPbI_3$ thin films (doping ratio in wt% of 1 mmol stock solution). (c) Normalized PL data of metal doped thin films.

for optical measurement were encapsulated with a 1 mg/ml stock solution of PMMA dissolved in chlorobenzene (CB) to avoid degradation from the air[23]. The UV-Vis-NIR spectroscopy was employed to measure the absorbance of the doped materials. The α-$CsPbI_3$ films showed a bandgap of ~1.73 eV, while Ba, Sb, and Sr doped thin films showed insignificant blue-shifts towards lower wavelength. Also, Sn doped thin films showed a similar cut-off wavelength to α-$CsPbI_3$, but Bi-doped thin films showed a slight red-shift towards higher wavelength, as shown in **Figure 3.1b**. The

bandgap calculations carried out with the Vienna Ab initio simulation package (VASP)[2] are shown in **Tables S3-S4**. The experimental bandgap values do not match exactly but shows a good correlation with the theoretical values. The photoluminescence (PL) spectra of the α-$CsPbI_3$ thin film showed broad spectra with a peak emission at ~706 nm, while the metal doped thin films showed a slight blue shift of ~4 nm, except for Bi-doping, which showed a redshift of ~3nm (**Figure 3.1c**).

3.4.3. The XRD analysis

The XRD pattern of the simulated cubic structures verified the experimental results, as shown in **Figure 3.2a**. We performed the XRD characterization of the thin films without encapsulation, while ensuring the minimum exposure to air before loading them to the XRD holder. The similarities between the obtained experimental and simulation results were confirmed. In **Figure 3.2c,** the peaks near 14.5°, 21°, and 29° for Ba^{2+}, Sr^{2+}, and Sn^{2+} confirm the cubic phase, while the peaks split around 21° and 29° for Sb^{3+} and Bi^{3+} doped films confirm the distorted tetragonal phase in both theory and experiment.[6,10,13] Ba-doped sample showed a slight peak shift towards the lower 2θ values, which signifies the successful incorporation of larger Ba^{2+} cation inside the $[Pb_6]^{4-}$ octahedral[23] (**Figure 3.2d**). Sr^{2+} and Sn^{2+} doped thin films showed insignificant peak shifts as they have almost similar atomic radii with the Pb^{2+} cation. Sb^{3+} and Bi^{3+} doped thin-films showed significant shifts towards lower 2θ values, possibly due to separate octahedral formations by Bi and Sb dopants.

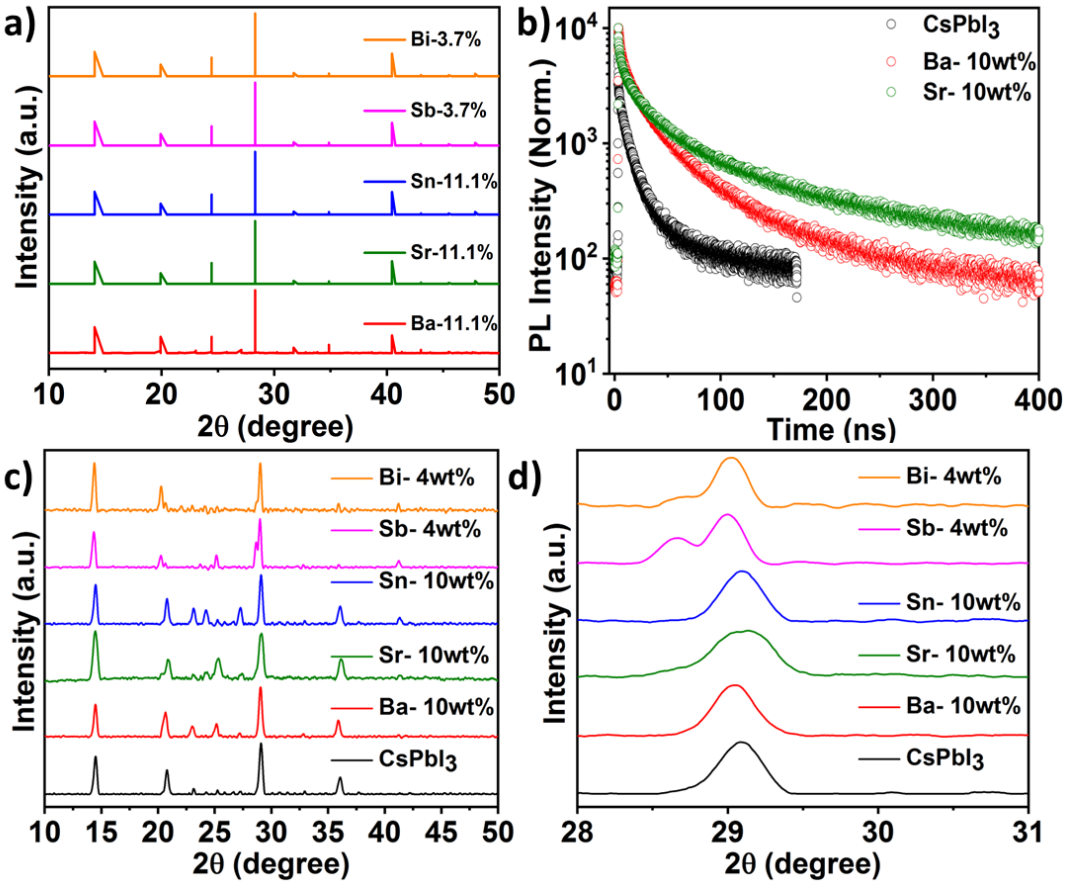

Figure 3.2. XRD results of the simulated structures and thin films of metal doped α-$CsPbI_3$ (a) Simulated patterns of the cubic structure in all doping schemes. (b) TCSPC results of α-$CsPbI_3$, Ba-10wt%, and Sr-10wt% doped thin films. (c) XRD patterns of the thin films of α-$CsPbI_3$ and doped one. (d) XRD patterns to verify the peak split for the Sb^{3+} and Bi^{3+} samples.

3.4.4. Time-correlated single photon counting (TCSPC) analysis

Time-correlated single photon counting (TCSPC) data were recorded to analyze the effect of doping on carrier lifetime. Herein, we were able to record it for α-$CsPbI_3$, Ba, and Sr doped samples (**Figure 3.2b**), but due to lower PL intensity of Sn^{2+} , Sb^{3+} and Bi^{3+} thin film samples, we were unable to record these lifetime. The average PL decay time (τ_{avg}) for α-$CsPbI_3$, Ba, and Sr doped samples were 11.55, 27.98, and 42.44 ns, respectively (**Table S5**). The τ_{avg} exhibited the improved charge dissociation and transport for the Sr doped thin film compared with α-$CsPbI_3$ and Ba doped thin films, so these results suggest that the Sr doped thin films are more suitable for device fabrication.

Table S5. Summary of the TCSPC results for α-$CsPbI_3$, Ba-10wt%, and Sr-10wt% doped thin films.

Sample	τ_1 (ns)	f_1(%)	τ_2 (ns)	f_2(%)	$\tau_{(avg)}$ (ns)	χ^2
Ref	7.03	77.94	22.06	27.51	11.55	1.20
Ba	13.07	64.84	55.46	35.16	27.98	1.50
Sr	16.22	67.70	97.37	32.30	42.44	1.55

τ_1: fast component relaxation time showing the presence of defect states, τ_2: slow component relaxation time showing effective recombination lifetime, τ_{avg}: average photoluminescence decay time, f_1 and f_2: relative contribution of component **1** & **2**, χ^2: chi square value.

3.4.5. Field emission scanning electron microscopy

Field emission scanning electron microscopy (FESEM) images reveal the effect of doping on the $CsPbI_3$ thin film surface morphology, as shown in **Figure 3.3.** The $CsPbI_3$ thin films confirm the inhomogeneous crystal size ranging between 200-500 nm without any pinhole. Here, it is important to mention that pinholes usually arise from the deposition process errors. Also, Ba doped thin films showed precipitated thin films with 100-200 nm grain size, while Sr doped thin films showed crystal with grain size ~100 nm, blended with ~50 nm grains. Furthermore, Sn doping films showed homogeneous nm range grain size, which seems to be precipitated from the top view. Furthermore, Sb doped thin films showed well-crystallized thin films, ranging from ~120–140 nm, while Bi-doped thin films showed better crystals among all the dopants ranging ~80–100 nm. The schematic of the

simulated structure is shown in **Figure 3.4a-f**, which illustrates the variations in α-$CsPbI_3$ crystal lattice after doping with various metals.

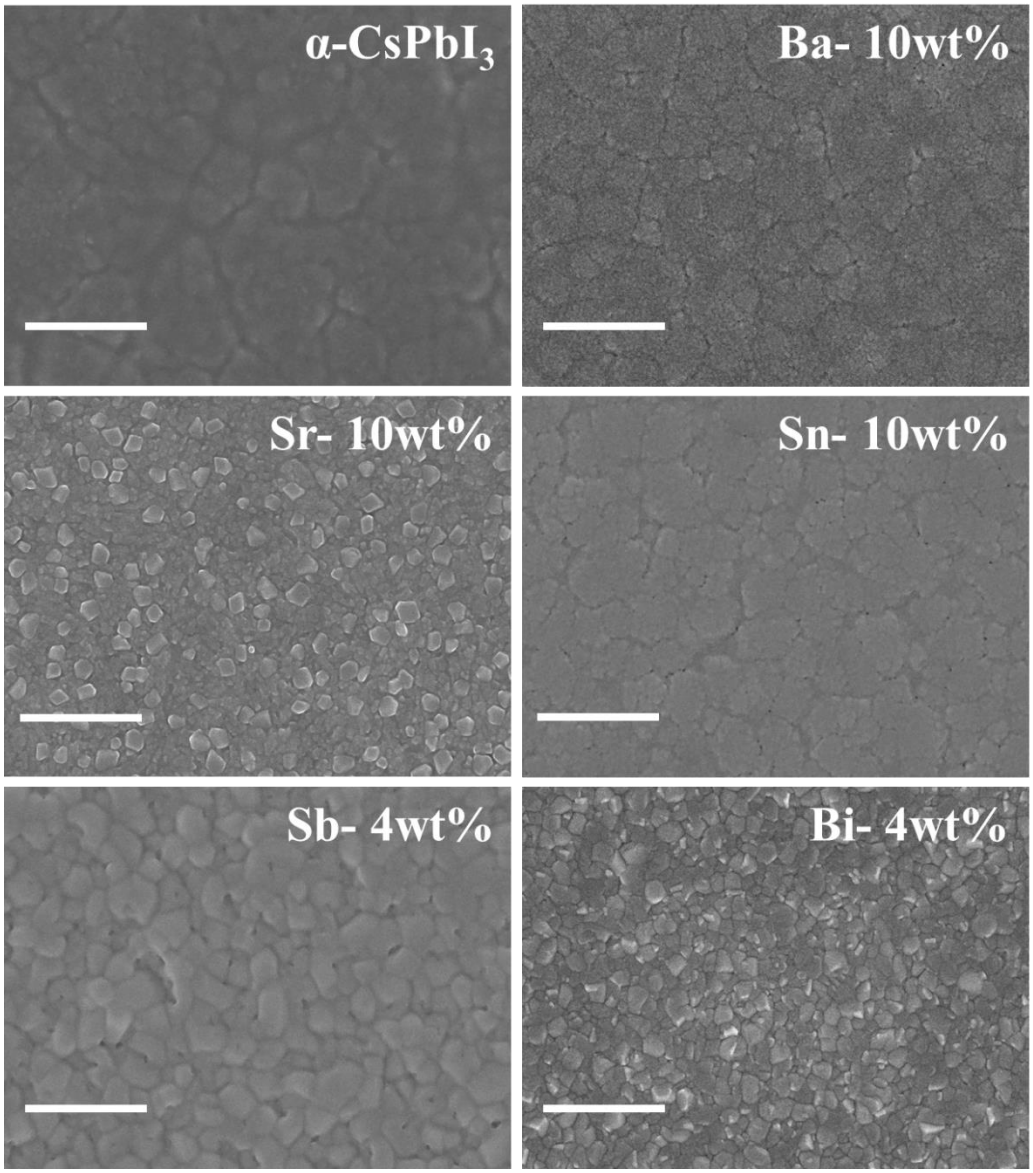

Figure 3.3. SEM images of the α-$CsPbI_3$ and doped thin films marked with doping concentration (scale bar 500 nm).

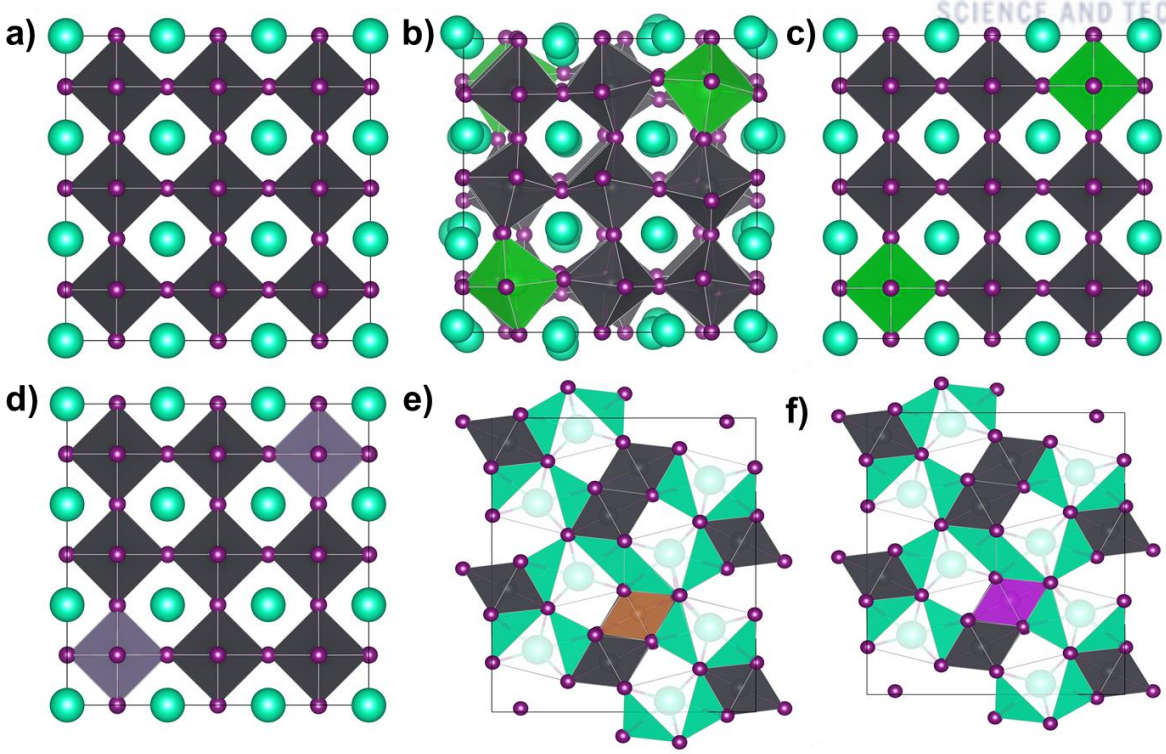

Figure 3.4. Structural schematic of the crystal structures obtained from DFT calculations (a) $CsPbI_3$, (b) $CsPb_{0.889}Ba_{0.111}I_3$, (c) $CsPb_{0.889}Sr_{0.111}I_3$, (d) $CsPb_{0.889}Sn_{0.111}I_3$, (e) $CsPb_{0.968}Sb_{0.032}I_3$, and (f) $CsPb_{0.968}Bi_{0.032}I_3$.

3.4.6. X-ray photoelectron spectroscopy

We performed X-ray photoelectron spectroscopy (XPS) to study the influence of metal doping on the elemental composition at the surface of the $CsPbI_3$ perovskite structure.[24,25] The Ba $3d_{5/2}$ and $3d_{3/2}$ characteristic peaks were observed at 779.5 and 794.5 eV, respectively (**Figure 3.5a**). The $3d_{5/2}$ and $3d_{3/2}$ characteristic peaks of Sr (136.8 and 137.2 eV in **Figure 3.6**), Sn (486.5 and 495.2 eV in **Figure 3.5b**), and Sb (531.7 and 539.1 eV in **Figure 3.5c**) were observed. The Bi $4f_{7/2}$ and $4f_{5/2}$ characteristic peaks were observed at 158.4 and 163.7 eV, respectively (**Figure 3.5d**). The XPS characteristics of Pb 4f, Cs 3d, and I 3d are explained in the supplementary information (**Figures 3.7-3.9**).

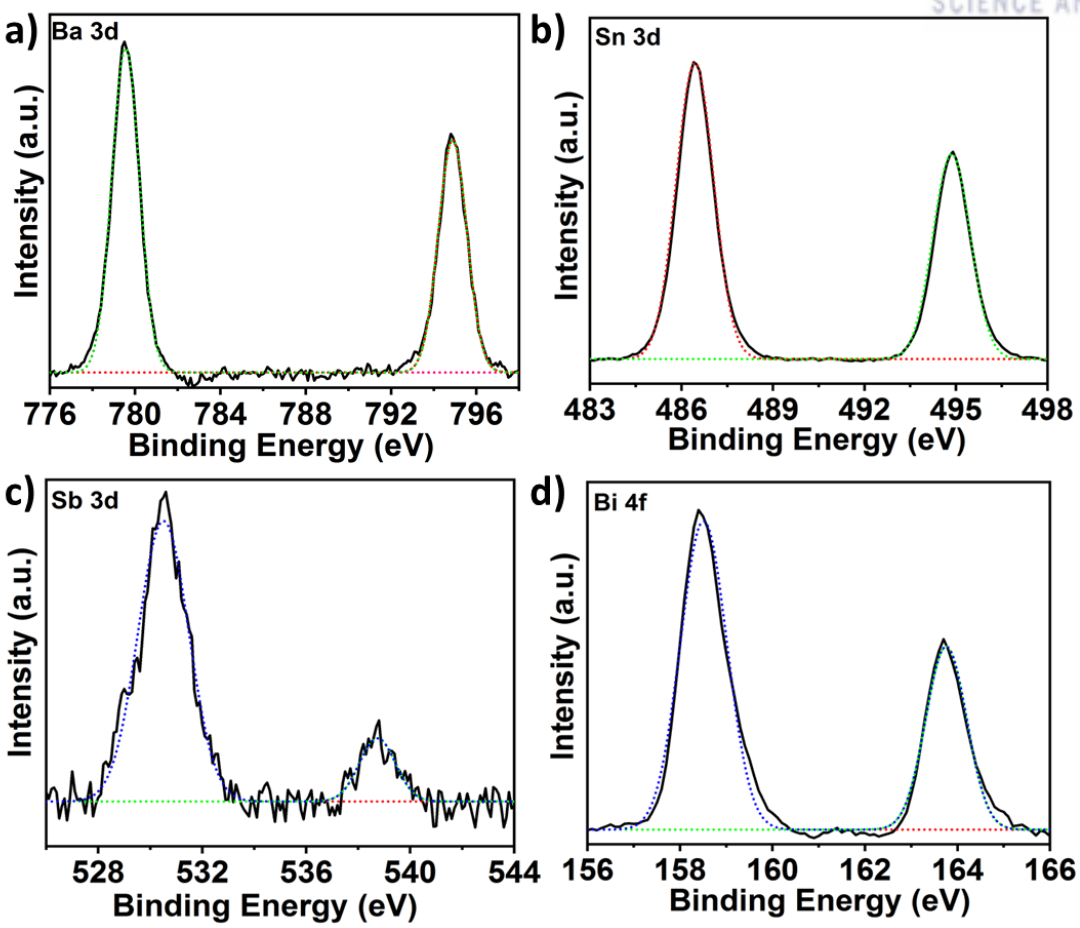

Figure 3.5. XPS spectra for (a) Ba 3d, (b) Sn 3d, (c) Sb 3d, and (d) Bi 4f.

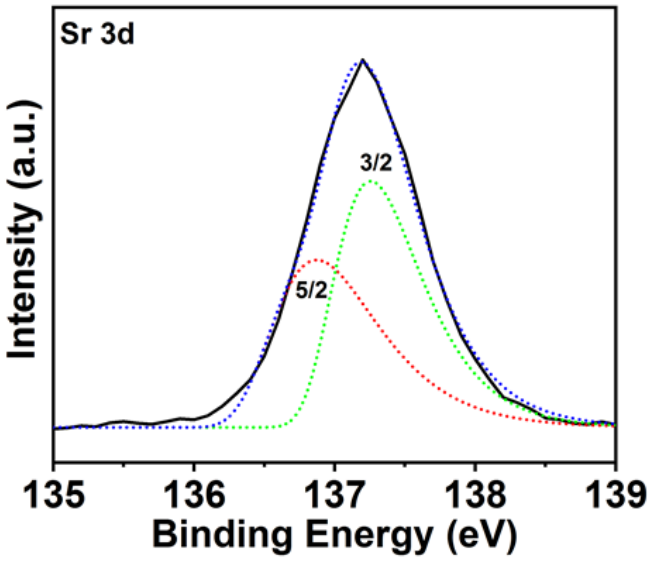

Figure 3.6. XPS spectra for Sr 3d in Sr doped α-$CsPbI_3$.

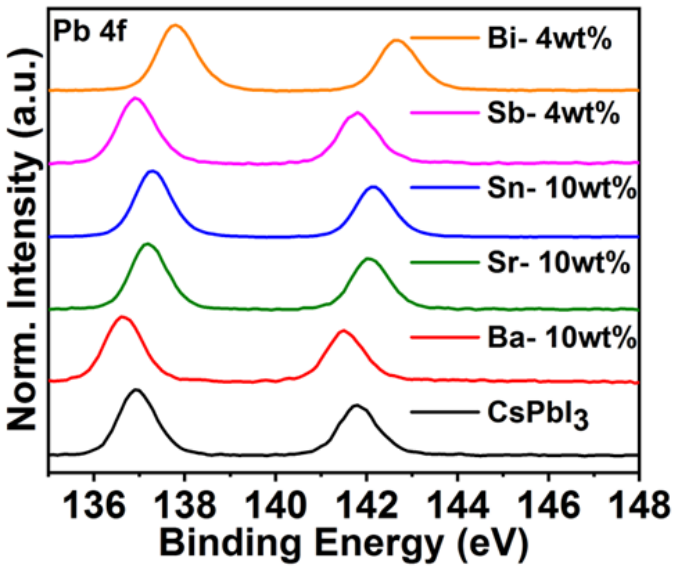

Figure 3.7. XPS spectra for Pb 4f of α-$CsPbI_3$, Ba-10wt%, Sr-10wt%, Sn-10wt%, Sb-4wt% and Bi-4wt% doped $CsPbI_3$.

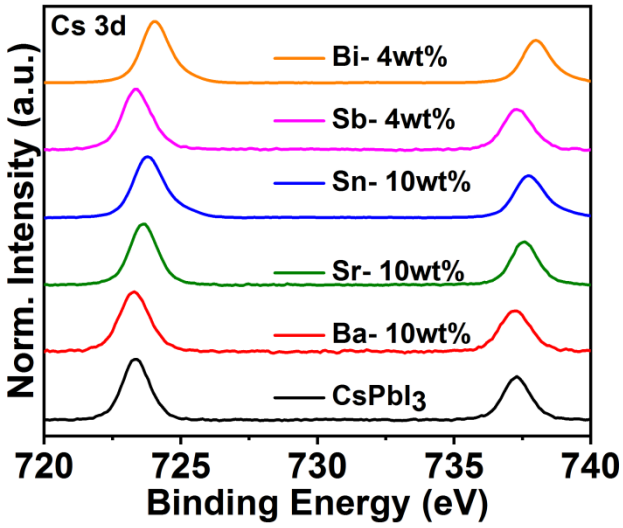

Figure 3.8. XPS spectra for Cs 3d of α-$CsPbI_3$, Ba-10wt%, Sr-10wt%, Sn-10wt%, Sb-4wt% and Bi-4wt% doped $CsPbI_3$.

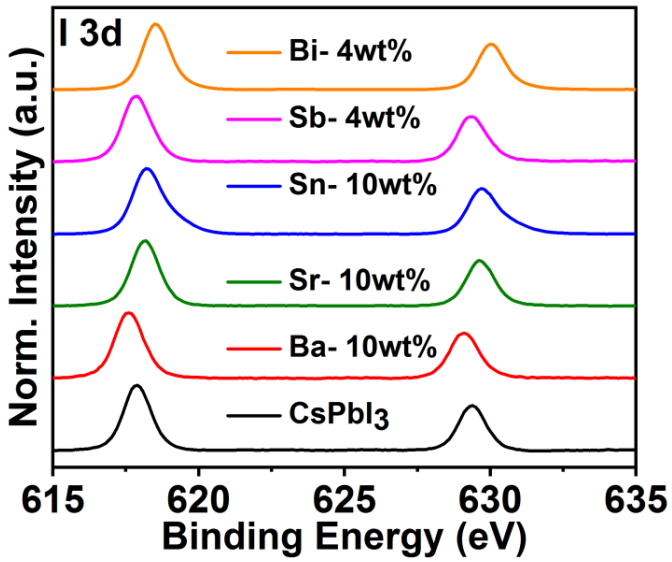

Figure 3.9. XPS spectra for I 3d of α-$CsPbI_3$, Ba-10wt%, Sr-10wt%, Sn-10wt%, Sb-4wt%, and Bi-4wt% doped $CsPbI_3$.

Conclusion

Here, we challenged the earlier reports of α-phase stabilization of $CsPbI_3$ by doping with Bi^{3+} and Sb^{3+}, and provided theoretical and experimental results to support our claim. We stabilized α-$CsPbI_3$ with Sr^{2+} metal doping for the first time without substituting Br^- or HI. In summary, we unfolded the effect of metal dopants with different valance states on the phase stablization of $CsPbI_3$. We conclude that the divalent metal cations (ie., Ba^{2+}, Sr^{2+}, and Sn^{2+}) stablize the α-phase of $CsPbI_3$ by replacing the Pb^{2+} atoms inside the crystal lattice, while heterovalent cations (i.e., Sb^{3+} and Bi^{3+}) stablize the β-phase of $CsPbI_3$ by inducing a stress on the crystal lattice, but these dopants cannot replace the Pb^{2+} sites. In addition, divalent metal-stabilized α-$CsPbI_3$ thin films are highly thermally stable compared to α-$CsPbI_3$ and heterovalent metal-stabilized β-$CsPbI_3$. When annealing above 100°C, the α-$CsPbI_3$/Sb^{3+}/Bi^{3+}-stabilized β-$CsPbI_3$ thin films turns back to photo-inactive yellow phase, while Ba^{2+}/Sr^{2+}/Sn^{2+}-stabilized α-$CsPbI_3$ thin films maintain their black phase. Also, the effect of metal doping on surface morphology, chemical composition and carrier lifetimes were successfully studied by measuring optical and chemical composition change with doping metals, and we also calculated band gaps with metal doping using DFT calculations. Furthermore, the effect of metal doping on air stability was observed by keeping the thin films outside the glove-box. The α-$CsPbI_3$ and its Ba, and Sr doped thin films maintain black phase for about 1 h, while Sb, Sn and Bi thin films maintain black phase for 5-6 h. Importantly, as alkali metals are more prone to oxidation, Ba and Sr thin films are oxidized easily, while Sb and Bi metals are less susceptible to oxidation and maintain black phase comparatively for more time. In short, Sn doped thin films are more air stable among all dopants, because Sn^{2+} donates electrons to the oxidizing Pb^{2+}. The much improved charge dissociation and

transport for the Sr doped thin film compared with α-$CsPbI_3$ and Ba doped thin films suggest that the Sr doped thin films are more suitable for device fabrication. Finally, we found that metal doped α-$CsPbI_3$ has the potential to provide thermally stable, highly efficient future optoelectronic devices. This study will provide new platform for improving air stability using additive assisted methods.

References

[1] Y. Wang, T. Zhang, M. Kan, Y. Zhao, *J. Am. Chem. Soc.* 2018, *140*, 12345.

[2] Y. Wang, M. I. Dar, L. K. Ono, T. Zhang, M. Kan, Y. Li, L. Zhang, X. Wang, Y. Yang, X. Gao, Y. Qi, M. Grätzel, Y. Zhao, *Science.* 2019, *365*, 591.

[3] Q. Wang, X. Zheng, Y. Deng, J. Zhao, Z. Chen, J. Huang, *Joule* 2017, *1*, 371.

[4] Q. Wang, X. Zheng, Y. Deng, J. Zhao, Z. Chen, J. Huang, *Joule* 2017, *1*, 371.

[5] J. Liang, X. Han, J. H. Yang, B. Zhang, Q. Fang, J. Zhang, Q. Ai, M. M. Ogle, T. Terlier, A. A. Martí, J. Lou, *Adv. Mater.* 2019, *31*, 1.

[6] S. Xiang, Z. Fu, W. Li, Y. Wei, J. Liu, H. Liu, L. Zhu, R. Zhang, H. Chen, *ACS Energy Lett.* 2018, *3*, 1824.

[7] B. Li, Y. Zhang, L. Fu, T. Yu, S. Zhou, L. Zhang, L. Yin, *Nat. Commun.* 2018, *9*, 1.

[8] R. J. Sutton, M. R. Filip, A. A. Haghighirad, N. Sakai, B. Wenger, F. Giustino, H. J. Snaith, *ACS Energy Lett.* 2018, *3*, 1787.

[9] A. Marronnier, G. Roma, S. Boyer-Richard, L. Pedesseau, J. M. Jancu, Y. Bonnassieux, C. Katan, C. C. Stoumpos, M. G. Kanatzidis, J. Even, *ACS Nano* 2018, *12*, 3477.

[10] Y. Kang, S. Kang, S. Han, *Mater. Today Adv.* 2019, *3*, DOI 10.1016/j.mtadv.2019.100019.

[11] Z. Li, F. Zhou, Q. Wang, L. Ding, Z. Jin, *Nano Energy* 2020, *71*, 104634.

[12] W. Xiang, Z. Wang, D. J. Kubicki, W. Tress, J. Luo, D. Prochowicz, S. Akin, L. Emsley, J. Zhou, G. Dietler, M. Grätzel, A. Hagfeldt, *Joule* 2019, *3*, 205.

[13] Y. Hu, F. Bai, X. Liu, Q. Ji, X. Miao, T. Qiu, S. Zhang, *ACS Energy Lett.* 2017, *2*, 2219.

[14] C. F. J. Lau, X. Deng, J. Zheng, J. Kim, Z. Zhang, M. Zhang, J. Bing, B. Wilkinson, L. Hu, R. Patterson, S. Huang, A. Ho-Baillie, *J. Mater. Chem. A* 2018, *6*, 5580.

[15] J. Liang, P. Zhao, C. Wang, Y. Wang, Y. Hu, G. Zhu, L. Ma, J. Liu, Z. Jin, *J. Am. Chem. Soc.* 2017, *139*, 14009.

[16] C. F. J. Lau, M. Zhang, X. Deng, J. Zheng, J. Bing, Q. Ma, J. Kim, L. Hu, M. A. Green, S. Huang, A. Ho-Baillie, *ACS Energy Lett.* 2017, *2*, 2319.

[17] T. Zhang, M. I. Dar, G. Li, F. Xu, N. Guo, M. Grätzel, Y. Zhao, *Sci. Adv.* 2017, *3*, 1.

[18] Y. Wang, X. Liu, T. Zhang, X. Wang, M. Kan, J. Shi, Y. Zhao, *Angew. Chemie - Int. Ed.* 2019, *58*, 16691.

[19] A. K. Jena, A. Kulkarni, Y. Sanehira, M. Ikegami, T. Miyasaka, *Chem. Mater.* 2018, *30*, 6668.

[20] L. Protesescu, S. Yakunin, M. I. Bodnarchuk, F. Krieg, R. Caputo, C. H. Hendon, R. X. Yang, A. Walsh, M. V. Kovalenko, *Nano Lett.* 2015, *15*, 3692.

[21] J. Lin, M. Lai, L. Dou, C. S. Kley, H. Chen, F. Peng, J. Sun, D. Lu, S. A. Hawks, C. Xie, F. Cui, A. P. Alivisatos, D. T. Limmer, P. Yang, *Nat. Mater.* 2018, *17*, 261.

[22] Y. Zhou, J. Chen, O. M. Bakr, H. T. Sun, *Chem. Mater.* 2018, *30*, 6589.

[23] S. Kajal, G. H. Kim, C. W. Myung, Y. S. Shin, J. Kim, J. Jeong, A. Jana, J. Y. Kim, K. S. Kim, *J. Mater. Chem. A* 2019, *7*, 21740.

[24] M. Deepa, M. Salado, L. Calio, S. Kazim, S. M. Shivaprasad, S. Ahmad, *Phys. Chem. Chem. Phys.* 2017, *19*, 4069.

[25] F. Matteocci, Y. Busby, J. J. Pireaux, G. Divitini, S. Cacovich, C. Ducati, A. Di Carlo, *ACS Appl. Mater. Interfaces* 2015, *7*, 26176.

[26] G. Kresse, J. Furthmüller, *Comput. Mater. Sci.* 1996, *6*, 15.

[27] J. P. Perdew, K. Burke, M. Ernzerhof, 1996, 3865.

Chapter 4

Halide-Free Passivating Material for Organic-Inorganic Perovskite Solar Cells

4.1. Abstract

The bulk perovskite crystals interface is a critical pathway for I^- ion migration, which induces current-voltage hysteresis in perovskite materials, as well as it decreases the stability of the perovskite solar cells. Terminating the I^- ion migration towards the electrodes, and passivating the surface defects improved the device performance, and stability of the perovskite solar cells. Here, we report a novel grain boundary passivation strategy by incorporating three different octyl-ammonium sulfate compounds. Octylamine functionalized with sulfanilic acid (OAS), p-toluene sulfonic acid (OAT), and camphor sulfonic acid (OAC) are synthesized and employed for grain boundary passivation. We demonstrate that, passivating the grains interface reduces the hysteresis, improved the charge recombination, and also improved the power conversion efficiency from **20.4% for the control to 20.8, 20.6, and 21%** for the devices treated with OAS, OAT, and OAC, respectively. The champion device exhibits a loss in efficiency of only **5%** under full sunlight intensity with maximum power tracking for **500 h**.

4.2. Introduction

Mixed cation hybrid lead halide perovskite solar cells paved the way towards long-term stability and efficient photovoltaic technologies. Recently, solution-processed lead halide perovskite solar cells surpassed the counterpart costly thin film fabrication technologies based solar cells (i.e. CIGS, and CdTe) with an attractive efficiency of 25.2%[1–5]. Easy and low-cost fabrication compared to the established Si-based photovoltaic technology is among the specific advantages that prompted the intensive research efforts to achieve efficient perovskite solar cells. Surface defect passivation, material composition, optimization of the device architecture, and the thin film thickness are the key deriving components towards higher efficiency. However, instability and surface defects incurred by grain boundary are still persistent in the polycrystalline perovskite thin films[6]. The polycrystalline perovskite thin films are fabricated by the spin coating process, and it undergoes the nucleation and growth after the solvent is evaporated from the precursor solution, there is an inhomogeneous growth, and it forms various surface defects, which leads to non-radiative recombination defects in perovskite. Jiang et al. reported that the surface, crystal grain boundaries and bulk point defects are responsible for ion migration[2]. Also, Xiao et al.'s study on switchable photovoltaic revealed that the large grain films are difficult to switch than small-grain films and they concluded that the ion migration might be dominated by the grain boundaries in polycrystalline thin films[7]. During the thermal annealing process, partial organic species might evaporate from the grain boundaries that leave the open space at grain boundaries. These GBs are suspected to be the channel for iodide (I^-) migration when electrical

potential is applied, the I^- ion accumulate towards the electrodes which create iodide vacancies[8]. The I^- ion accumulation towards negative electrode induces hysteresis behavior which suggest a decomposition of the perovskite material under long term operation[9]. Therefore, various efforts have been done for the passivation of grain boundaries, including 2D/3D interfacing, alkylammonium post treatment, alkylamines and wide bandgap halides coating, etc[1–3,5,10]. The post-treatment decreased the hysteresis in the device to some extent; incorporation of fluorocarbon-based bifunctional molecules improved the performance by 53.3% and reached a PCE of 21.31% in the champion device[11]. The Voc of the best performing device increased from 1.11 V for the reference device to the 1.14 V for passivated device. Furthermore, passivating with ethylammonium, imidazolium, and guanidinium iodide in mixed cation halide perovskite improved the efficiency to 22.3%, 22.1%, and 21%, respectively, compared to 20.5% for the control device. The open circuit voltage increased with an average gain of 30 mV, 70 mV, and 40 mV for ethylammonium, imidazolium, and guanidinium iodide, respectively. The increase in Voc indicates the reduced charge recombination and champion device exhibit reduced hysteresis compared to the control device. The passivation material forms microstructures with the unreacted PbI_2 at the interface. Also, the best performing device maintained efficiency of up to 95% under full sun light with maximum power tracking for 550 hours. Jung et al. reported that deposition of wide-bandgap light-absorbing material (*n*-hexyl trimethylammonium bromide) layer on the perovskite surface. They achieved a certified PCE of 22.7% with hysteresis of ±0.51%; also the device exhibited excellent stability at 85% relative humidity without encapsulation; and with encapsulation the device exhibited long term stability for 1370 hours under 1-sun condition with a drop of only 5% compared with its maximum power tracking. Moreover, the coating of wide-bandgap halide improved the Voc to 1.145 mV as compared with the Voc of 0.925 mV for the control device[1].

Herein, we report a halide free passivation strategy to stop accumulation of I^- towards Au, we show that treating the grain boundaries in perovskite material with newly synthesized octylammonium sulfate compounds such as OAS, OAT, and OAC improved the device performance. We used mixed cation/halide perovskite formulations of the composition ($Fa_{0.85}MA_{0.15}PbI_{0.85}Br_{0.85}$). This surface passivation improved the optical properties of the perovskite layer; also the hysteresis was reduced to insignificant. We characterized the surface treated perovskite thin films using XPS, NMR, and compared them with the control perovskite thin films to study the interface effect.

4.3. Materials and methods

4.3.1. Chemicals and Reagents: Octylamine (99.9%), (1S)-(+)-10-camphor sulfonic acid (CSA, 99%), sulfanilic acid (Sulf, 99%), p-tolunesulfonic acid (PTSA, 99%), methyammonium bromide (anhydrous, ≥99.9%), lead iodide (PbI_2,99.9%), dimethyl sulfoxide (DMSO, anhydrous, 99.8%),

Spiro-MeOTAD (99%), chlorobenzene (CB, anhydrous 99.8%) and all other chemicals including N,N-dimethylformamide (DMF, anhydrous, 99.8%) were purchased from Sigma-Aldrich. All salts and solvents were used as received without any further purification.

4.3.2. Synthesis of Octylammonium Sulfonate Compounds: The octylamine ($CH_3(CH_2)_6CH_2NH_2$) (99%) was reacted with sulfanilic acid (PTSA, 99%) by slowly adding in 1:1 mmol ratio. Similarly, octylamine was reacted with p-toluenesulfonic acid monohydrate (PTSA, 99%), and (1S)-(+)-10-camphor sulfonic acid (CSA, 99%) to synthesize their compounds at 20°C for 3 hours. The obtained slurry was dissolved in warm methly alcholol and then recrystallized with diethyl ether[16]. The obtained final product was washed with diethyl ether. Finally, the final product was filtered and dried at 60 °C in a vaccum oven for 24 hours.

4.3.2. Solar Cell Fabrication: Firstly, we ultrasonically cleaned the substrate by detergent, deionized water, acetone, and isopropyl alcohol for 20 min each, and then treated it by a UV/O_3 cleaner for 30 minutes. Then, the SnO_2 layer was spin-coated on the glass/ITO substrates, followed by annealing at 150°C for 15 minutes. After depositing the electron transport layer, the perovskite layer was deposited by two-step spin coating method using the 1.5 mM perovskite precursor solution having $(FaPbI_3)_{0.85}(MaPbBr3)_{0.15}$, where PbI_2 precursor dissolved in DMF was coated at the speed of 5000 rpm for 30 s, and $FA_{0.85}MA_{0.15}$ dissolved in isopropyl alcohol (IPA) was coated at 3000 rpm for 30 s, and annealed at 150°C for 15 minutes. On top of the perovskite layer, the passivation layer dissolved IPA was coated at 5000 rpm, and annealed at 100°C for 10 minutes. Later, the HTL layer of Spiro solution was spin-coated at 3000 rpm for 30 s. Finally, 80-nm thick gold electrode as the top electrode was deposited through the shadow mask using thermal evaporation, with an active area of 0.130 cm^2.

4.3.3. Characterization and measurements: A digital source meter (Keithley 2635A) was used to measure Current density–voltage (*J–V*) characteristics of the solar cells. Solar cell performance was measured under illumination by an Air Mass 1.5 Global (AM 1.5 G) solar simulator with an irradiation intensity of 100 mW cm^{-2}. Apertures (13.0 mm^2) made of thin metal were attached to each cell before measurement for *J–V* characteristics. The device stability was measured in time step. External quantum efficiency (EQE) measurements were obtained with a PV measurements QE system under ambient conditions, with monochromated light from a xenon arc lamp. The monochromatic light intensity was calibrated with a Si photodiode and chopped at 100 Hz. The absorption preoperties of thin film were characterized by UV-Vis-NIR (Carry 5000, Agilent) while thin film PL was measure with Fluorometer (Carry Eclipse, Agilent) excited at 450 nm The surface morphologies of perovskite with/without additive were analyzed by field emission SEM (Nova NanoSEM, FEI). The crystallographic information was determined by high power XRD (MAX 2500V, Rigaku) using Cu Kα radiation (λ = 1.54059 Å) with scanning angle 2θ ranging from 10° and 60°. Chemical composition of the sample were investigated by XPS (K-alpha, ThermoFisher) while, Elemental

compostion distribution measurement was carried out in depth profiling mode using TOF SIMS 5 (ION TOF) and the thickness of the samples were measured by surface profiler (KLA Tencor).

4.4. Results

4.4.1. PSC fabrication and characterization

We synthesized three different Octyl-ammonium sulfate compounds, where octylamine reacted with sulfanlic acid, p-toluene sulfonic acid, and camphor sulfonic acids were named as Sulf, PTSA, and CSA respectively. While, the thin films passivated with Sulf, PTSA, and CSA were abbreviated as OAS, OAT, and OAC, as shown in **Figure 4.1**. We employed a halide free passivation layer on top of perovskite layer, our device architecture comprises a indium tin oxide (ITO) conducting glass substrate, on top of which, we deposited a compact ~20 nm thin SnO_2 layer followed by Perovskite/passivation layer/Spiro-OMeTAD/Au. The device fabrication procedure is detailed in the method section. The perovskite layers were annealed at 150°C for 30-40 min. After cooling down the perovskite layer, the passivation layer was coated by spin coating on top of the perovskite layer and annealed at 70°C for 10 minutes. The concentration of the passivation layer compounds was optimized and compared at their best.

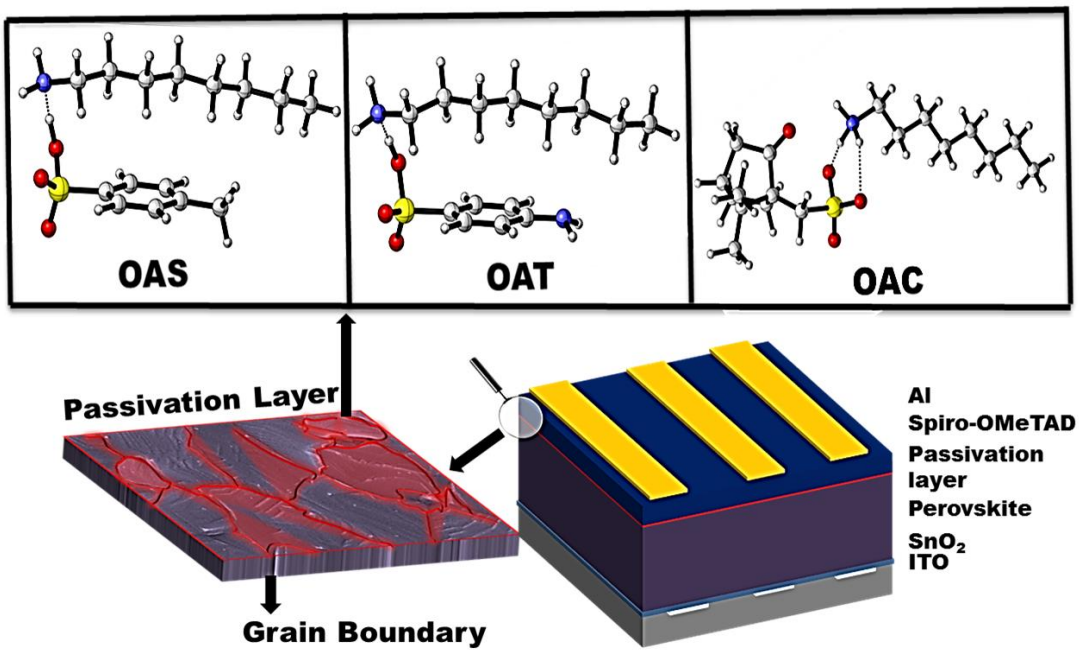

Figure 4.1. Schematic representation of passivation scheme and the fabricated device structure.

4.4.2. Solid state magic angle spinning NMR

Alharbi et al. demonstrated that solid state magic angle spinning (MAS) NMR can be used to probe atomic level microstructures at the perovskite and passivation layer interface[3]. We carried out solid-

state NMR characterization to probe the formation of octylamine functionalized with various sulfonic acids and atomic-level microstructure of passivated lead halide perovskite. The OAS sample has a broad ^{1}H-^{1}H proton coupling, significant by two broad peaks at 8.24 and 1.08 ppm, having full-width half maximum (FWHM) of 2.7 and 1.8 ppm, which indicates a strong 1H-1H dipole coupling in (NH) and (CH) proton environment. Importantly, a broad peak at 8.24 ppm covers the OH, NH_2 and NH_3 regions, which indicates an exchange of protons with other labile protons (OH protons). Also, the peak intensity of NH protons is higher compared to the CH protons. While in the OAT sample, the ^{1}H-^{1}H proton coupling region separated between two regions having two peaks in each region. The NH proton region has broad peaks at 8.28 and 7.46 (CH) ppm, while the CH proton region has broad peaks at 2.85 (CH_2) and 1.68 (CH_3) ppm[12]. Where, the effect of CH_2 tail at the end of PTSA, can be observed as an increase in CH proton intensity compared to the NH protons intensity. In the OAC sample, the signature peak at 8.24 ppm has an FWHM of 1.6 ppm, while the CH proton region has a broad and intense peak at 3.6, 1.82, and 1.44 ppm. The broad CH proton peak has higher proton density and it indicates an intermediate proton exchange rate among these species. The control perovskite film identifies the presence of two organic species at 4.10 (CH_2) and 1.68 (CH_3) ppm, while there are no significant unreacted N-H proton peaks that can represent strong coupling but there is a negligible broad peak in this region[10]. Solid-state NMR of passivated thin films show significant signature peaks, which strengthens our hypothesis of ionic interaction between the perovskite and passivation layer. The C-H bond observes chemical shift in OAS, OAT, and OAC treated thin films to 1.73 ppm (CH_3), also the presence of unreacted octylamine tail give signal at 1.30 and 0.9 ppm in OAS treated sample. Similarly, OAT observes these peaks at 1.50 and 1.24 ppm and OAC samples have peak at 1.30 ppm. The presence of octylamine tail peaks in passivated films signifies the change in structural orientation of the passivation material after coating onto perovskite layer, which gives rise to separate C-H bond peaks compared to the synthesized material. Also, chemical shift in CH_2 peak in treated perovskite films were observed compared to control films, which signifies lower proton density in that region from the untreated films. Most importantly, all passivated thin films have similar broad signature peak in O-H, phenyl and **N-H** bond region at 8.7 (OH), 7.9 (NH_2) and 6.8 (NH_3) ppm with a variation in peak intensity. The NH_2^+, CH_3, and CH_2 in FA and sulfonated compound are correlated to each other and are microscopically mixed within the same phase.

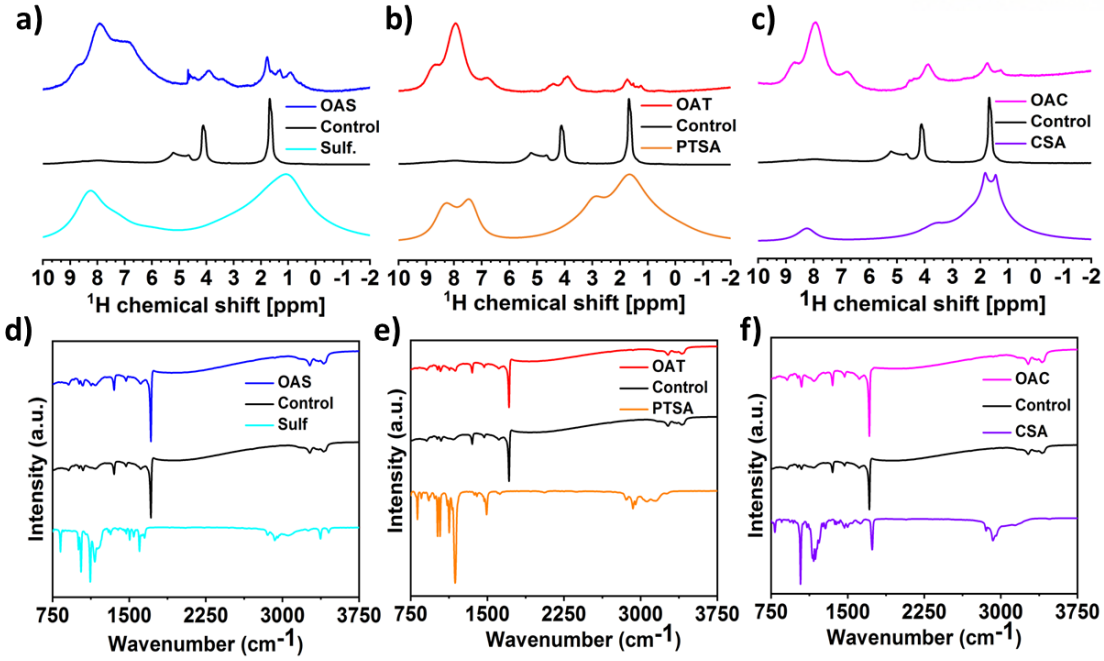

Figure 4.2. Solid state NMR spectroscopy and FT-IR results of the passivated thin films and synthesized material. a-c) NMR results of thin films in powder form, d-f) FT-IR results of the

4.4.3. Fourier-transform infrared spectroscopy

Glaser et al. demonstrated that infrared spectroscopy can be used to probe the vibrational mores in perovskite materials, we performed fourier-transform infrared spectroscopy (FT-IR) for the synthesized materials and the passivated perovskite thin films shown in figure 2 a-c. We observed intense (C–H) bending peaks at 824 cm^{-1} and 1027 cm^{-1} for Sulf sample, while a slight shift to higher frequencies for PTSA and CSA was observed. These peaks correspond to out of plane bending of C–H bond and CH_3–NH_3^+, respectively. Also, the S=O stretching peaks were observed at 1304 cm^{-1} for Sulf, while intense peaks with significant shift to higher frequency where observed for PTSA and CSA samples. Additionally, an asymmetrical absorption for NH_3^+ was observed around 1500 cm^{-1} in all the synthesized materials. Furthermore, in all the synthesized materials the symmetrical and asymmetrical CH_3 peaks were observed around 2854 and 2925 cm^{-1}, respectively. Moreover, symmetrical NH_3^+ peaks were observed for PTSA and CSA around 3145 cm^{-1} and shifted peaks towards higher frequency were observed for Sulf sample at 3371 cm^{-1}. Finally, the absence of O-H stretching peaks in the synthesized powder samples indicates the formation of the octylammonium sulfonated compounds; also it indicated the reaction at the target site. However, control, OAS, OAT, and OAC thin films samples show similar absorbance peaks at 1350 cm^{-1} for symmetrical CH_3 bend, while NH_3^+ peaks were observed at 1710, 3240, and 3400 cm^{-1}, the thickness of passivation layer is

insignificant compared to the perovskite layer, so it is hard to differentiate the peaks arising from the passivation material.

4.4.4. Structural and optical properties

The interaction between the passivation layer and the perovskite layer traced by X-ray diffraction (XRD), which reveals insignificant change in the perovskite crystallographic structure. The reference samples reveal unreacted PbI_2 (2θ = 12.7°), while passivated samples have no excess PbI_2 peak (**Figure 3a**), which indicates that the unreacted PbI_2 at the interface makes ionic complex with NH_3^+ tail[3]. UV-Vis spectra of the control sample exhibited insignificant red shift at absorption onset with OAS, OAT, and OAT samples, which is assumed as the effect of ionic complex made by the passivation material at the top of the perovskite layer, as shown in **Figure 3b**. Also, we investigated the steady-state and time-resolved photoluminescence (PL) of the control and the passivated perovskite layers. **Figure 3c** show an increase in the PL intensity of the passivated samples, which suggests a reduction of the non-radiative recombination losses that could be explained by the reduction in surface defects by the passivation layer. Also, the surface passivated thin films exhibited an inconsiderable blueshift, which might be the result of ionic complex at the top of the perovskite layer.

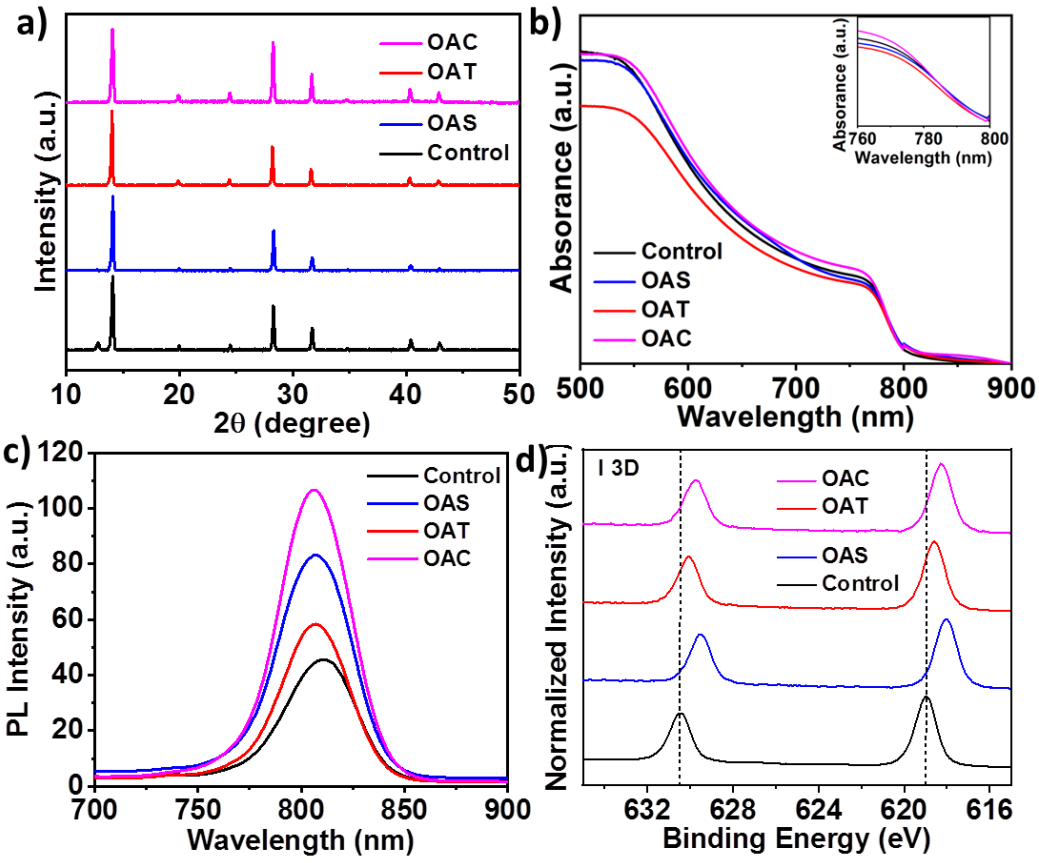

Figure 4.3. Structural and optical properties of the passivated thin films. a) Xrd pattern of the control and passivated thin films, b) UV-vis absorption spectra, c) Photoluminescence d) XPS spectra for I 3d.

4.4.5. Surface morphology analysis

The surface images of the perovskite films were recorded via scanning electron microscopy (SEM), as shown in **Figure 4**. In our study, the mixed cation perovskite layer was used as a control device, and the films coated with the three synthesized compounds were compared to examine the passivation of the perovskite grain boundary. Herein, we infer that all the samples have similar large grains ranging between ~600-900 nm. From the SEM images, it is evident that the control sample has large grain boundaries, and also have few pinholes, formed during crystallization. These grain boundaries are filled by the three compounds, and no pinhole is evident from the surface images. There was complete surface coverage of the perovskite layer after using the optimized concentration. However, from the SEM images, it is evident that the surface morphology of the passivation layer changes with the change in sulfonic acid group. OAS and OAT covers the whole perovskite layer while rod like shape in OAT hampers the whole surface passivation. We also investigated the surface roughness of passivation layer coated thin films using atomic force microscopy (AFM), as shown in **Figure X**. It is evident that the thin films with passivation layers are smoother compared to the control thin film. Therefore, the increase of surface smoothness resulted in smaller contact areas at the interface, which decreases the trap states and enhances the wettability of the HTL layer leading to an increase in Jsc.

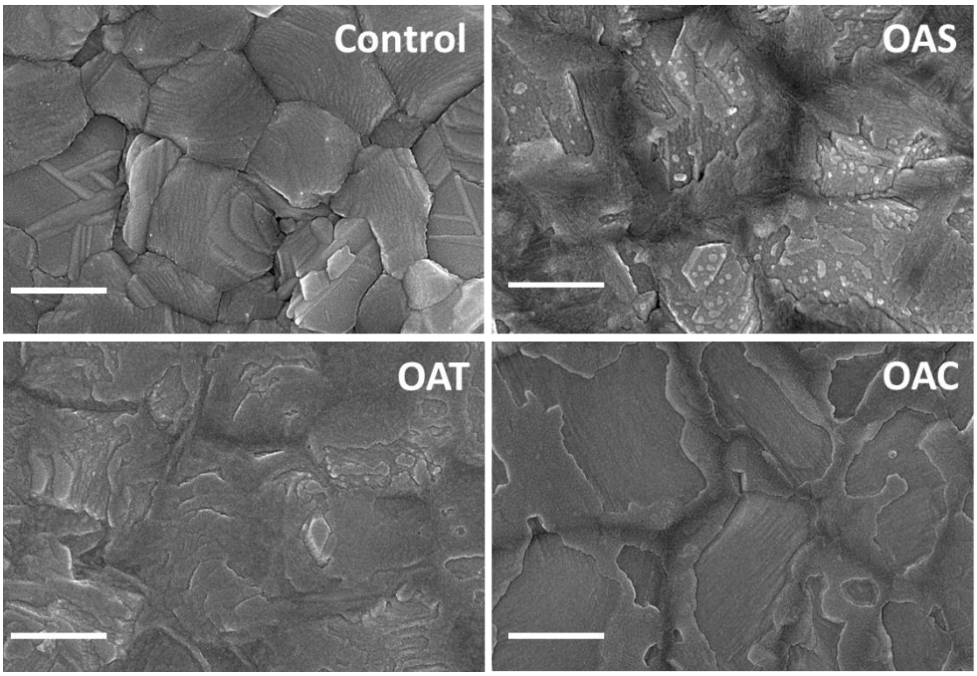

Figure 4.4. SEM images of the control and passivated thin films.

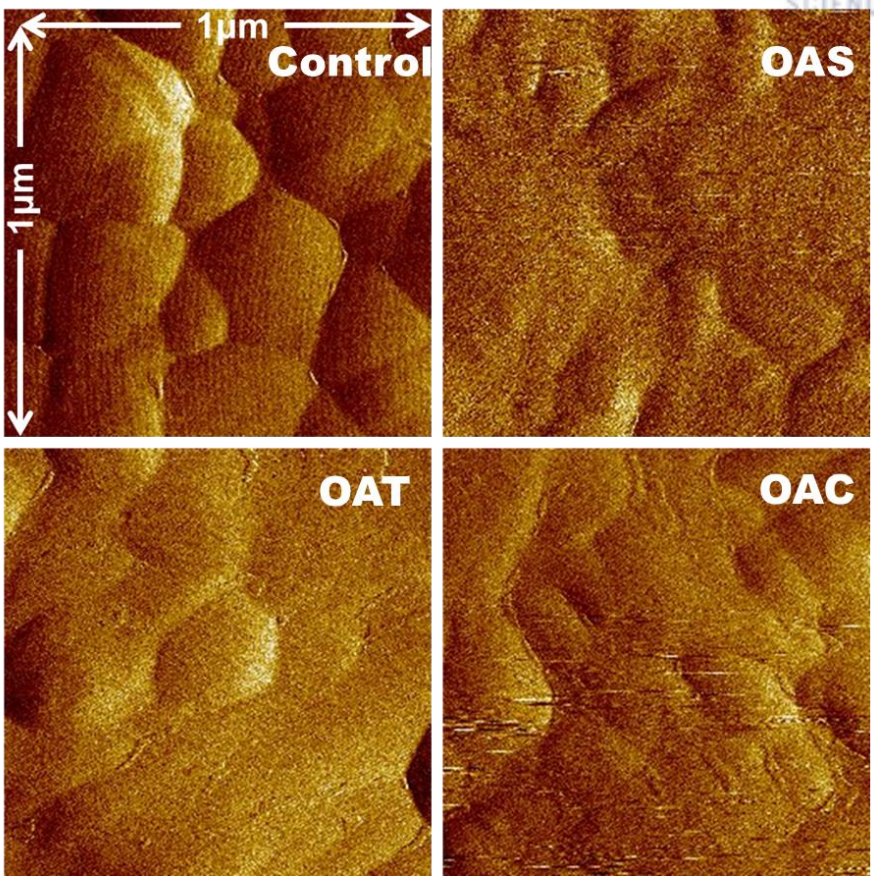

Figure 4.5. AFM images of the control and passivated thin films.

4.4.6. X-ray photoelectron spectroscopy

We compared the effect of surface passivated thin films with the control films by using X-ray photoelectron spectroscopy to elucidate the effects on Pb^0 and I^0 defects. As shown in **Figure 4.6**, the binding energy of control films at 142.8 and 138.0 eV were assigned to $4f_{5/2}$, $4f_{7/2}$ of divalent Pb^{2+}, respectively, while, passivated thin films binding observes significant shift towards lower energies at 142.1 and 137.0 eV in $4f_{5/2}$, $4f_{7/2}$ peaks, which can be understood by dissimilar electronegativity at the interface. Passivation materials have lower electronegativity compared to the perovskite material which leads to a decrease in binding energy. Also, intensity of the peak Pb^{2+} peaks decreases after passivation which indicates the diffusion of atoms towards the bulk perovskite rather than the passivation layer. The binding energy of control films at 630.4 and 618.9 eV were assigned to $3d_{3/2}$, $3d_{5/2}$ of divalent I^-, respectively. Similarly, all passivated thin films binding observes shift towards lower energies and there is no indication of I^0 species upon fitting, which shows that I^- are well preserved in the bulk perovskite, as shown in **Figure 4.3d.** Though our study focused on improving the grain boundary defects, we also tried to emphasize on eliminating the pathway for I^- ion migration.

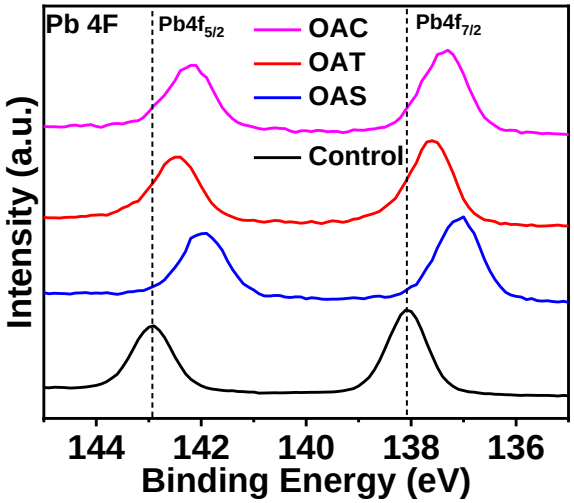

Figure 4.6. XPS spectra for Pb 4f.

4.5. Photovoltaic device and performance

To validate the effect of the surface passivation by ammonium salt series for the complete devices, we measured J-V characteristic for PeSCs devices without and with OAS, OAT, OAT passivation layer under 1.5G illumination at 100 mW cm^{-2}. The PSCs devices were prepared with the architecture of the ITO/SnO_2/perovskite layer/passivation layer/Spiro-OMeTAD/Au. The average power conversion efficiency increased from 18.56% for the control device to 18.26%, 22.09%, and 21.5% for OAS, OAT, and OAC, respectively.

4.6. References

1. Jung, E. H. *et al.* Efficient, stable and scalable perovskite solar cells using poly(3-hexylthiophene). *Nature* **567**, 511–515 (2019).

2. Jiang, Q. *et al.* Surface passivation of perovskite film for efficient solar cells. *Nat. Photonics* **13**, 460–466 (2019).

3. Alharbi, E. A. *et al.* Atomic-level passivation mechanism of ammonium salts enabling highly efficient perovskite solar cells. *Nat. Commun.* **10**, 1–9 (2019).

4. Wang, L. *et al.* A Eu 3+ -Eu 2+ ion redox shuttle imparts operational durability to Pb-I perovskite solar cells. *Science (80-.).* **363**, 265–270 (2019).

5. Min, H. *et al.* Efficient, stable solar cells by using inherent bandgap of a-phase formamidinium lead iodide. *Science (80-.).* **366**, 749–753 (2019).

6. Jung, M., Shin, T. J., Seo, J., Kim, G. & Seok, S. Il. Structural features and their functions in surfactant-armoured methylammonium lead iodide perovskites for highly efficient and stable solar cells. *Energy Environ. Sci.* **11**, 2188–2197 (2018).

7. Xiao, Z. *et al.* Giant switchable photovoltaic effect in organometal trihalide perovskite devices. *Nat. Mater.* **14**, 193–197 (2015).

8. Yuan, Y. & Huang, J. Ion Migration in Organometal Trihalide Perovskite and Its Impact on Photovoltaic Efficiency and Stability. *Acc. Chem. Res.* **49**, 286–293 (2016).

9. Li, C. *et al.* Iodine Migration and its Effect on Hysteresis in Perovskite Solar Cells. *Adv. Mater.* **28**, 2446–2454 (2016).

10. Kubicki, D. J. *et al.* Cation Dynamics in Mixed-Cation (MA)x(FA)1-xPbI3 Hybrid Perovskites from Solid-State NMR. *J. Am. Chem. Soc.* **139**, 10055–10061 (2017).

11. Guo, P. *et al.* Surface & grain boundary co-passivation by fluorocarbon based bifunctional molecules for perovskite solar cells with efficiency over 21%. *J. Mater. Chem. A* **7**, 2497–2506 (2019).

12. Ruiz-Preciado, M. A. *et al.* Supramolecular Modulation of Hybrid Perovskite Solar Cells via Bifunctional Halogen Bonding Revealed by Two-Dimensional 19F Solid-State NMR Spectroscopy. *J. Am. Chem. Soc.* **142**, 1645–1654 (2020).

13. Rocks, C., Svrcek, V., Maguire, P. & Mariotti, D. Understanding surface chemistry during MAPbI3 spray deposition and its effect on photovoltaic performance. *J. Mater. Chem. C* **5**, 902–916 (2017).

14. Taucher, T. C., Hehn, I., Hofmann, O. T., Zharnikov, M. & Zojer, E. Understanding Chemical versus Electrostatic Shifts in X-ray Photoelectron Spectra of Organic Self-Assembled Monolayers. *J. Phys. Chem. C* **120**, 3428–3437 (2016).

15. Kajal, S. *et al.* A thermally stable, barium-stabilized α-CsPbI3 perovskite for optoelectronic devices. *J. Mater. Chem. A* **7**, 21740–21746 (2019).

16. Yoon, T. *et al.* Ambient-Stable Cubic-Phase Hybrid Perovskite Reaching the Shockley–Queisser Fill Factor Limit via Inorganic Additive-Assisted Process. *ACS Appl. Energy Mater.* **1**, 5865–5871 (2018).

Acknowledgment

Firstly, I would like to thank God for everything he bestowed me. I would like to express my sincere gratitude to my advisor Prof. Kwang Soo Kim, for his strong support, insightful guidance, and supervision throughout my doctoral study. I am thankful for his critical comments and advice during my Ph.D. degree, which helped me a lot to solve the research problems. I'm glad to have the supervision of such a knowledgeable professor. I would also express my appreciation to Dr. Atanu Jana and Dr. Gi-Hwan Kim for their guidance, great help, and helpful discussions. I'm grateful to Prof. Jin Young Kim to allow me to work in his lab, and also I'm thankful to all his students for their support.

I would like to thank my thesis committee members: Prof. Jin Young Kim, Prof. Tae-Hyuk Kwon, Prof. Geunsik Lee, and Prof. Gi-Hwan Kim for their evaluation, insightful comments, and advice during the examination of the Ph.D. thesis and defense. I am thankful for all my labmates and administrative staff of the center for superfunctional materials UNIST for their support. I'm thankful to my family members for their life long support, without their support it was not possible to achieve this goal. I had a good time with friends at UNIST and I'm very grateful to all of them. I would like to thank all my friends and supervisors in India who motivated me to set and achieve such a prestigious goal in my life. Finally, I would like to thank my parents for their deep understanding, support, and love. I highly appreciate their patience, sacrifice, and prayers for my success.